



Modeling anisotropic flow and heat transport by using mimetic finite differences

Tao Chen*, Christoph Clauser, Gabriele Marquart, Karen Willbrand, Henrik Büsing

Institute for Applied Geophysics and Geothermal Energy, E.ON Energy Research Center, RWTH Aachen University, Mathieustr. 10, D-52056 Aachen, Germany



ARTICLE INFO

Article history:

Received 30 November 2015

Revised 9 June 2016

Accepted 10 June 2016

Available online 14 June 2016

Keywords:

Mimetic finite differences

Flow

Heat transport

Equivalent fracture permeability

Full permeability tensor

Heterogeneity

ABSTRACT

Modeling anisotropic flow in porous or fractured rock often assumes that the permeability tensor is diagonal, which means that its principle directions are always aligned with the coordinate axes. However, the permeability of a heterogeneous anisotropic medium usually is a full tensor. For overcoming this shortcoming, we use the mimetic finite difference method (mFD) for discretizing the flow equation in a hydrothermal reservoir simulation code, SHEMAT-Suite, which couples this equation with the heat transport equation. We verify SHEMAT-Suite-mFD against analytical solutions of pumping tests, using both diagonal and full permeability tensors. We compare results from three benchmarks for testing the capability of SHEMAT-Suite-mFD to handle anisotropic flow in porous and fractured media. The benchmarks include coupled flow and heat transport problems, three-dimensional problems and flow through a fractured porous medium with full equivalent permeability tensor. It shows firstly that the mimetic finite difference method can model anisotropic flow both in porous and in fractured media accurately and its results are better than those obtained by the multi-point flux approximation method in highly anisotropic models, secondly that the asymmetric permeability tensor can be included and leads to improved results compared the symmetric permeability tensor in the equivalent fracture models, and thirdly that the method can be easily implemented in existing finite volume or finite difference codes, which has been demonstrated successfully for SHEMAT-Suite.

© 2016 Elsevier Ltd. All rights reserved.

1. Introduction

Modeling anisotropic flow through heterogeneous or fractured porous media is required for subsurface energy production and environmental protection, such as production of hydrocarbons (e.g., Srinivasan and Azom, 2013) and geothermal energy (e.g., Llanos et al., 2015), groundwater resource management (e.g., Dickson et al., 2014), waste disposal (e.g., McKenna et al., 2003), and CO₂ sequestration (e.g., Kumar et al., 2005).

Due to the complexity in geologic processes, anisotropic permeability occurs on various scales and varies with time (Manga et al., 2012), as demonstrated in various experimental, numerical, and theoretical studies: on a small scale, mineral grains and micro-cracks orient along a preferential direction during rock formation or due to stress (e.g., Wright et al., 2009; Bolton et al., 2000). On a medium scale, joints or fractures are created under crustal stress or by hydraulic fracturing, providing preferable flow paths (Snow, 1969; Min et al., 2004; Aghighi and Rahman, 2010). On a large scale, anisotropic permeability in sediments results from het-

erogeneities with preferred orientations (Makse et al., 1996; Lewis, 1988) or from faults (Zhang and Tullis, 1998; Farrell et al., 2014).

Mathematically, anisotropic permeability in Darcy flow is usually described by a tensor (e.g., Bear, 1972). The heterogeneity of geological properties, such as porosity (Hu et al., 2009) and permeability (Meyer and Krause, 2006), the complexity of boundary conditions, and the coupling of flow, heat, stress, and chemical reactions (e.g., Domenico and Schwartz, 1998) usually requires numerical methods for solving subsurface flow problems (e.g., Aziz and Settari; 1979, Gessner et al., 2009; Miller et al., 2013). The finite volume method (two-point flux approximation) has been used widely in commercial simulators due to its simple seven-point stencil (in three dimensions) and robust convergence and monotonicity. The method assumes a diagonal permeability tensor requiring the main axes of the permeability tensor to be always aligned with the coordinate axes of the model domain. However, when using full permeability tensors with non-zero symmetric or asymmetric off-diagonal terms (Durlofsky, 2005; Zijl, 1996; Chen et al., 2015), solutions based on this method will be incorrect.

In the past two decades, some schemes have been developed and applied for overcoming this shortcoming (Verma and Aziz, 1997; Droniou, 2014). In the multi-point flux approximation

* Corresponding author. Fax: +492418049889.

E-mail address: chentao9330@gmail.com (T. Chen).

(MPFA) finite volume method (Aavatsmark et al., 1996; Edwards and Rogers, 1998), the flux on the grid faces is calculated from more than two grid points. Extensions of this method, the MPFA-O and MPFA-U methods (Aavatsmark et al., 1996), MPFA-L method (Aavatsmark et al., 2008), MPFA-G method (Agélas et al., 2010), MPFA-Z method (Nordbotten and Eigestad, 2005) and enriched MPFA method (Chen et al., 2008a) were developed for improving the monotonicity of the solution. The last characters in the names of the different MPFA methods are related to the shapes of the stencils used for flux computation. For dealing with a full permeability tensor while maintaining the simplicity of the two-point flux approximation method, a nonlinear two-point flux approximation method was developed (Chen et al., 2008b; Nikitin et al., 2014) using a nonlinear relation for calculating flux between the two points. The mimetic finite difference method (Lipnikov et al., 2014) can also model flow through porous or fractured media with a full permeability tensor. Some applications for isothermal reservoir simulation are presented in Aarnes et al. (2008); Alpak (2010); Lipnikov et al. (2011), and Nilsen et al. (2012). Li et al. (2010) developed a 3D steady flow simulator with full hydraulic conductivity tensors using a 19-point finite difference method. Arnaldsson et al. (2014) used a new scheme for modeling flow through anisotropic rocks using a horizontal full permeability tensor.

For accurate modeling flow within highly anisotropic porous or fractured porous media in non-isothermal processes, more robust numerical methods are needed. In this paper, we apply the mimetic finite difference method for the coupled flow and heat transport equations. Full permeability tensors only concern flow problems and fluid properties vary with temperature. Furthermore, we use asymmetric full permeability tensors, which may arise during upscaling procedures, for the equivalent fracture models. Lastly, we apply the mimetic finite difference method to general groundwater related problems, such as a highly heterogeneous model and a three-dimensional model in which the anisotropies are different between two layers. For exemplifying our approach, we use a parallelized modular version of SHEMAT (Clauer, 2003), SHEMAT-Suite (Rath et al., 2006), a simulator for modeling reactive flow in hot reservoirs. However, the approach can be applied to any finite-difference or finite-volume flow simulator.

This paper is organized as follows: first we present the governing equations for flow and heat transport in the simulator SHEMAT-Suite and introduce the mimetic finite difference discretization for the flow equation. Then, we illustrate the flow chart of the implementation. In the third part, SHEMAT-Suite-mFD is verified against analytical solutions of pumping tests. Finally, three benchmarks are performed and compared, testing the capability of the new scheme with respect to coupling of flow and heat transport in both a homogeneous and a highly heterogeneous model, to three-dimensional problems with both diagonal and full tensor permeability, and to equivalent fracture models involving a full permeability tensor.

2. Equations and discretization

2.1. Flow equation

The specific discharge (or Darcy velocity) \mathbf{v} in a porous medium can be expressed by:

$$\mathbf{v} = -\frac{\rho_f g \mathbf{k}}{\mu} (\nabla h_0 + \rho_r \nabla z), \quad (1)$$

where ρ_f denotes actual (temperature and pressure dependent) fluid density, g gravity, \mathbf{k} the rock permeability tensor, μ actual fluid dynamic viscosity, h_0 hydraulic constant density reference head; h_0 is computed from elevation z , fluid pressure P , fluid den-

sity at reference conditions, ρ_0 , and g as:

$$h_0 = z + \frac{P}{\rho_0 g}, \quad (2)$$

where ρ_r is the relative fluid density given by:

$$\rho_r = \frac{\rho_f - \rho_0}{\rho_0}. \quad (3)$$

Mass conservation is expressed by:

$$S_s \frac{\partial h_0}{\partial t} = -\nabla \cdot \mathbf{v} + Q, \quad (4)$$

where t denotes time, Q is a volumetric source term and S_s the specific storage coefficient computed from fluid density, ρ_f , gravity, g , rock compressibility, α , fluid compressibility, β , and porosity, ϕ :

$$S_s = \rho_f g(\alpha + \phi\beta). \quad (5)$$

Combining Eqs. (1) and (4) yields the flow equation (e.g., Clauer, 2003):

$$S_s \frac{\partial h_0}{\partial t} = \nabla \cdot \left[\frac{\rho_f g \mathbf{k}}{\mu} (\nabla h_0 + \rho_r \nabla z) \right] + Q. \quad (6)$$

2.2. Heat transport equation

Similarly, the heat transport equation can be derived from energy conservation (e.g., Clauer, 2003):

$$(\rho c)_e \frac{\partial T}{\partial t} = \nabla \cdot (\lambda_e \nabla T) - \nabla \cdot [(\rho c)_f \mathbf{v} T] + H, \quad (7)$$

where $(\rho c)_e$ is the effective volumetric thermal capacity computed from fluid and rock densities, ρ_f and ρ_m , and specific heat capacities, c_f and c_m , and porosity ϕ :

$$(\rho c)_e = \phi \rho_f c_f + (1 - \phi) \rho_m c_m, \quad (8)$$

where T denotes temperature, λ_e is the effective thermal conductivity tensor computed from fluid and rock conductivities λ_f and λ_m weighted by porosity ϕ by a suitable mixing law, $(\rho c)_f$ is the fluid volumetric thermal capacity, and H is a heat generation source term.

Flow and heat transport (Eqs. 6) and (7), are dynamically coupled by the pressure and temperature dependence of the fluid and rock properties. In SHEMAT-Suite most of these dependencies are considered: in the flow Eq. (6), fluid density ρ_f , fluid compressibility β , and fluid viscosity μ may vary with pressure and temperature. In the heat transport Eq. (7), fluid density ρ_f , fluid thermal conductivity λ_f and fluid specific heat capacity c_f , depend on pressure and temperature, while rock thermal conductivity, λ_m , and specific heat capacity, c_m , depend on temperature only. Specific discharge in Eq. (7), \mathbf{v} , is obtained by solving the flow Eq. (6). Further details of the coupling and the code are discussed in Clauer (2003).

2.3. Mixed-hybrid finite element discretization of flow equation

The mimetic finite difference method shares many similarities with the mixed-hybrid finite element method (Brezzi and Fortin, 1991; Arbogast et al., 1997). We introduce the mimetic finite difference method from the viewpoint of the mixed-hybrid finite element method so that the difference between the two methods can be clearly presented.

Using the derivation steps by Lunde (2007), we start by transforming Eqs. (1) and (4) into their corresponding weak forms. The idea behind this is to relax the assumption of continuous differentiability and thus allow a wider set of possible solutions. After

defining a Sobolev space $H^{\text{div}}(\Omega)$, we multiply Eq. (1) with a continuous vector-valued function $\mathbf{w} \in H^{\text{div}}(\Omega)$ and integrate over the domain Ω :

$$\int_{\Omega} \mathbf{w} \cdot \left(-\frac{\mu}{\rho_f g} \mathbf{k}^{-1} \right) \mathbf{v} d\Omega = \int_{\Omega} \mathbf{w} \cdot (\nabla h_0 + \rho_r \nabla z) d\Omega. \quad (9)$$

By using Green's identity for the right-hand side, we obtain:

$$\begin{aligned} \int_{\Omega} \mathbf{w} \cdot (\nabla h_0 + \rho_r \nabla z) d\Omega &= \int_s (h_0 + \rho_r z) \mathbf{w} \cdot \mathbf{n} ds \\ &\quad - \int_{\Omega} (h_0 + \rho_r z) \nabla \cdot \mathbf{w} d\Omega. \end{aligned} \quad (10)$$

where s is the perimeter of Ω and \mathbf{n} is the outward normal unit vector. Thus, combining Eqs. (9) and (10) yields:

$$\int_{\Omega} \mathbf{w} \cdot \frac{\mu}{\rho_f g} \mathbf{k}^{-1} \mathbf{v} d\Omega = \int_{\Omega} (h_0 + \rho_r z) \nabla \cdot \mathbf{w} d\Omega - \int_s (h_0 + \rho_r z) \mathbf{w} \cdot \mathbf{n} ds. \quad (11)$$

We define $L^2(\Omega)$ as a space consisting of functions that are square-integrable. Similarly, multiplying Eq. (4) with a continuous scalar-valued function $\varphi \in L^2(\Omega)$ and integrating over the same domain, Ω , we get:

$$\int_{\Omega} \varphi S_s \frac{\partial h_0}{\partial t} d\Omega = \int_{\Omega} -\nabla \cdot \mathbf{v} \varphi d\Omega + \int_{\Omega} \varphi Q d\Omega. \quad (12)$$

Using the backward-in-time discretization:

$$\frac{\partial h_0}{\partial t} = \frac{h_0^n - h_0^{n-1}}{\Delta t}, \quad (13)$$

where h_0^n and h_0^{n-1} are the hydraulic constant density reference heads in the current and previous time steps, respectively, we substitute Eq. (13) into Eq. (12):

$$\int_{\Omega} \varphi S_s \frac{h_0^n}{\Delta t} d\Omega = \int_{\Omega} -\nabla \cdot \mathbf{v} \varphi d\Omega + \int_{\Omega} \varphi Q d\Omega + \int_{\Omega} \varphi S_s \frac{h_0^{n-1}}{\Delta t} d\Omega. \quad (14)$$

For Eqs. (11) and (14), we divide the domain Ω into N_E cuboids denoted as $\Omega_h = \bigcup_{i=1}^{N_E} E_i$, and introduce a set of bilinear forms to shorten the notation and for better readability (see Appendix A for their definitions). The mixed weak form of Eqs. (1) and (4) now reads as follows: find $(\mathbf{v}, h_0^n) \in H^{\text{div}}(\Omega_h) \times L^2(\Omega_h)$ such that:

$$\begin{aligned} b(\mathbf{w}, \mathbf{v}) - c(\mathbf{w}, h_0^n) &= (\nabla \cdot \mathbf{w}, \rho_r z) - (h_0 + \rho_r z, \mathbf{w} \cdot \mathbf{n}), \\ \forall \mathbf{w} \in H^{\text{div}}(\Omega_h), \end{aligned} \quad (15a)$$

$$c(\mathbf{v}, \varphi) + j(\varphi, h_0^n) = (\varphi, Q) + \left(\varphi, S_s \frac{h_0^{n-1}}{\Delta t} \right), \forall \varphi \in L^2(\Omega_h). \quad (15b)$$

The linear system arising from Eq. (15) is not positive-definite (Brezzi and Fortin, 1991). By applying the hybridization technique, we can obtain a symmetric positive-definite linear system of equations, which is not only easier to solve, but also contains more information (Cockburn et al., 2009). To this end, we define h_f^n , the hydraulic constant density reference head on the element faces denoted by $\partial\Omega_h$, and introduce bilinear forms $d(\cdot, \cdot)$ and a scalar-valued function $\eta \in L^2(\partial\Omega_h)$ (see Appendix A for the definition of $d(\cdot, \cdot)$). The mixed-hybrid weak form problem can be expressed now as: find $(\mathbf{v}, h_0^n, h_f^n) \in H^{\text{div}}(\Omega_h) \times L^2(\Omega_h) \times L^2(\partial\Omega_h)$ such that:

$$\begin{aligned} b(\mathbf{w}, \mathbf{v}) - c(\mathbf{w}, h_0^n) + d(\mathbf{w}, h_f^n) &= (\nabla \cdot \mathbf{w}, \rho_r z) - (h_0 + \rho_r z, \mathbf{w} \cdot \mathbf{n}), \\ \forall \mathbf{w} \in H^{\text{div}}(\Omega_h), \end{aligned} \quad (16a)$$

$$c(\mathbf{v}, \varphi) + j(\varphi, h_0^n) = (\varphi, Q) + \left(\varphi, S_s \frac{h_0^{n-1}}{\Delta t} \right), \quad \forall \varphi \in L^2(\Omega_h), \quad (16b)$$

$$d(\mathbf{v}, \eta) = (g^N, \eta), \quad \forall \eta \in L^2(\partial\Omega_h). \quad (16c)$$

Eq. (16) can be seen as a hybrid version of the mixed weak form Eq. (15) after introducing a new variable h_f^n which plays the role of Lagrange multipliers (Brezzi and Fortin, 1991) and adding Eq. (16c) to ensure the continuity of the specific discharge across the element faces.

The weak form Eq. (16) can be discretized by replacing $H^{\text{div}}(\Omega_h)$, $L^2(\Omega_h)$, and $L^2(\partial\Omega_h)$ with finite dimensional subspaces V , U , and Π . This is necessary since we want to solve the Eq. (16) eventually using finite computer arithmetic. Therefore, the mixed-hybrid finite element method reads: find $(\mathbf{v}, h_0^n, h_f^n) \in V \times U \times \Pi$ such that (16) holds for all $(\mathbf{w}, \varphi, \eta) \in V \times U \times \Pi$. The mixed-hybrid finite element method can be classified further with respect to different finite element spaces, e.g., Raviart-Thomas-Nédélec spaces (Raviart and Thomas, 1977; Nédélec, 1980); Brezzi-Douglas-Marini spaces (Brezzi et al., 1985); Brezzi-Douglas-Durán-Fortin spaces (Brezzi et al., 1987a); Brezzi-Douglas-Fortin-Marini spaces (Brezzi et al., 1987b); and Chen-Douglas spaces (Chen and Douglas, 1989).

2.4. Mimetic finite difference discretization of the flow equation

Although the original derivations are different, it has been recognized recently that the mimetic finite difference method is equivalent to the mixed-hybrid finite element method with the lowest-order Raviart-Thomas-Nédélec elements on regular grids (Droniou, 2014). However, the mimetic finite difference method is more flexible regarding the element shapes (Lipnikov et al., 2014). Derivation of the mimetic finite difference method from the viewpoint of the support operator method can be found in Shashkov and Steinberg (1996). Following the derivation of the mixed-hybrid finite element method shown above, we use the lowest-order Raviart-Thomas-Nédélec elements (Fig. 1a, see Appendix B for the definitions of the approximate subspaces V , U , and Π) and represent \mathbf{v} , h_0^n , and h_f^n by using the basis functions $\mathbf{w}_i \in V$, $\varphi_i \in U$, and $\eta_i \in \Pi$:

$$\mathbf{v} = \sum_{i=1}^{N_F} v_i \mathbf{w}_i, \quad (17a)$$

$$h_0^n = \sum_{i=1}^{N_E} h_{0i}^n \varphi_i, \quad (17b)$$

$$h_f^n = \sum_{i=1}^{N_{FI}} h_{fi}^n \eta_i, \quad (17c)$$

where N_F is the number of element faces by summing up those of each element, N_E is the total number of elements, and N_{FI} is the number of element faces by global ordering (Fig. 1c). The linear system arising from (17) can be written in matrix form:

$$\begin{bmatrix} \mathbf{M} & -\mathbf{C}^T & \mathbf{D}^T \\ \mathbf{C} & \mathbf{J} & 0 \\ \mathbf{D} & 0 & 0 \end{bmatrix} \begin{bmatrix} \mathbf{v} \\ \mathbf{h}_0^n \\ \mathbf{h}_f^n \end{bmatrix} = \begin{bmatrix} \rho_r \mathbf{z} - \mathbf{g}^D \\ \mathbf{Q} + \mathbf{S}_s \frac{\mathbf{h}_0^{n-1}}{\Delta t} \\ \mathbf{g}^N \end{bmatrix}, \quad (18)$$

where $\mathbf{M} = [b(w_j, w_i)]_{i,j=1,2,\dots,N_F}$, $\mathbf{C} = [c(w_j, \varphi_i)]_{i,j=1,2,\dots,N_E}$, $j = 1, 2, \dots, N_F$,

$$\mathbf{D} = [d(w_j, \eta_i)]_{i=1,2,\dots,N_{FI},j=1,2,\dots,N_F}, \quad \mathbf{J} = [j(\varphi_j, \varphi_i)]_{i,j=1,2,\dots,N_E},$$

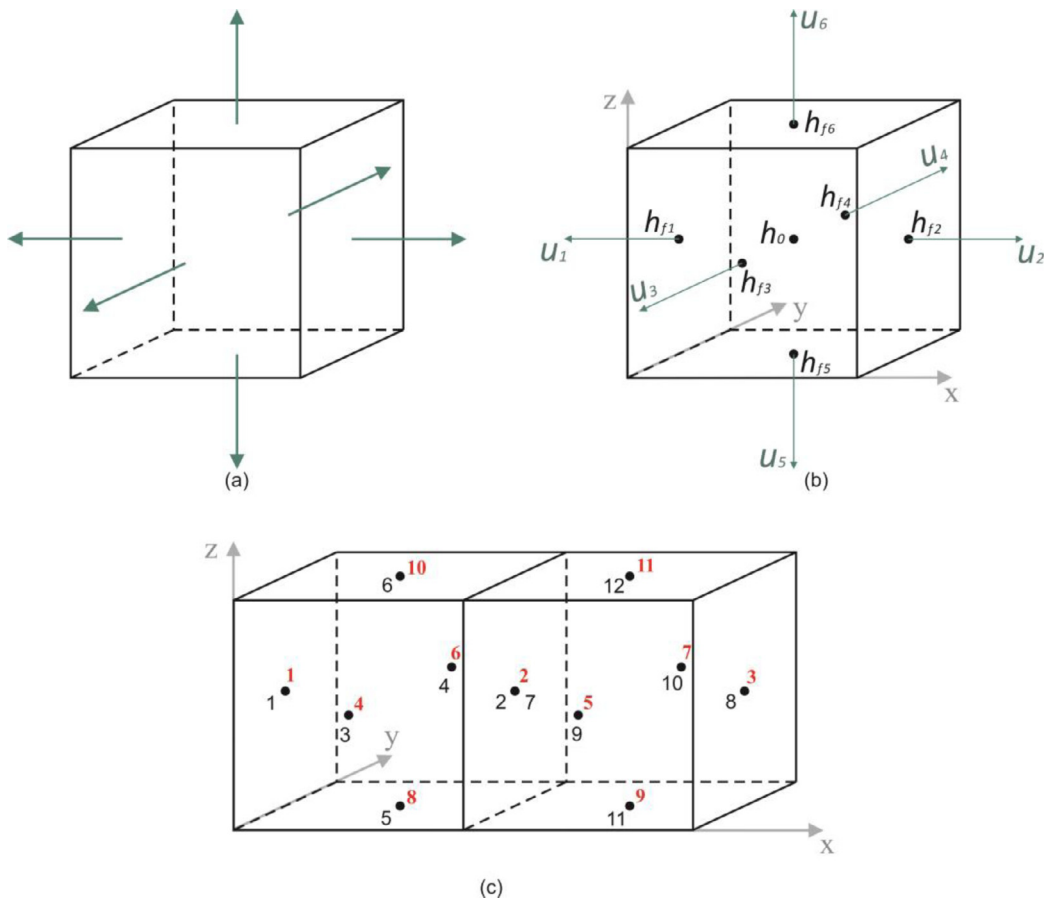


Fig. 1. (a) The lowest-order Raviart-Thomas-Nédélec element. Arrows represent the velocities on the faces. (b) The total discharge, u , the hydraulic heads, h_0 and h_f , and their ordering in an element in the mimetic finite difference method. (c) The local ordering, $N_F = 12$ in black numbers, and the global ordering, $N_{Fl} = 11$ in red numbers, for a two-element grid system. (For interpretation of the references to color in this figure legend, the reader is referred to the web version of this article.)

$$\begin{aligned}\mathbf{u} &= [u_i]_{i=1,2,\dots,N_F}, \quad \mathbf{h}_0^n = [h_{0i}^n]_{i=1,2,\dots,N_E}, \quad \mathbf{h}_f^n = [h_{fi}^n]_{i=1,2,\dots,N_E}, \\ \mathbf{Q} &= [(\varphi_i, Q_i)]_{i=1,2,\dots,N_E}, \quad \mathbf{S}_s \frac{\mathbf{h}_0^{n-1}}{\Delta t} = \left[\left(\varphi_i, \left(\mathbf{S}_s \frac{\mathbf{h}_0^{n-1}}{\Delta t} \right)_i \right) \right]_{i=1,2,\dots,N_E}, \\ \mathbf{g}^D &= [(h_0 + \rho_r z)_i, w_i \cdot n_i]_{i=1,2,\dots,N_F}, \quad \rho_r \mathbf{z} = [\nabla \cdot w_i, \rho_r z_i]_{i=1,2,\dots,N_F}, \\ \mathbf{g}^N &= [(g_i^N, \eta_i)]_{i=1,2,\dots,N_F}.\end{aligned}$$

Following Lie et al. (2012), we use a total discharge \mathbf{u} instead of the specific discharge \mathbf{v} in the linear Eq. (18). As the relationship between total discharge, \mathbf{u} , and specific discharge, \mathbf{v} , is $\mathbf{u} = \mathbf{v}A$, where A is the area of the element face, the matrices \mathbf{M} , \mathbf{C} , \mathbf{D} and \mathbf{g}^N in Eq. (18) related to \mathbf{v} will have slight changes regarding the area of the element face. The variables in the mimetic finite difference method are shown in Fig. 1b. Then, \mathbf{M} , \mathbf{C} and \mathbf{J} are block diagonal matrices that contain the matrices \mathbf{M}_i , the vector $\mathbf{e}_i = (1, 1, 1, 1, 1, 1)$, and the scalar $(\frac{S_s}{\Delta t})_i$ for each element E_i , respectively. The rows and columns of ones in \mathbf{D} correspond to the element faces in global ordering of the domain and their local ordering of each element, respectively (Fig. 1c).

The matrices \mathbf{M}_i are the key element of the mimetic finite difference method. It turns out that \mathbf{M}_i can be chosen from a family of matrices, which should satisfy both the stability and convergence criteria for the solutions (Brezzi et al., 2005). The mixed-hybrid finite element method with the lowest-order Raviart-Thomas-Nédélec elements can be created by a specific choice of

\mathbf{M}_i . We use the formula by Lie et al. (2012) for computing \mathbf{M}_i^{-1} , which will be used directly in the following solving process. For an element E_i , there is an associated matrix \mathbf{M}_i^{-1} of the form:

$$\mathbf{M}_i^{-1} = \frac{1}{|E_i|} \left[\mathbf{N}_i \mathbf{k}_i \mathbf{N}_i^T + \frac{6 \operatorname{tr}(\mathbf{k}_i)}{d_i} \mathbf{A}_i (\mathbf{I}_i - \mathbf{R}_i \mathbf{R}_i^T) \mathbf{A}_i \right], \quad (19)$$

where the matrix \mathbf{N}_i is computed from the area-weighted outward vector normal to the element face; \mathbf{k}_i is the permeability tensor, and $\operatorname{tr}(\mathbf{k}_i)$ is the trace of \mathbf{k}_i ; $|E_i|$ and d_i are the volume and dimension of the element E_i , respectively; \mathbf{A}_i is a diagonal matrix computed from element face areas; \mathbf{I}_i is the identity matrix; \mathbf{R}_i is an orthonormal basis for the matrix \mathbf{Z}_i , $\mathbf{Z}_i = \mathbf{A}_i \mathbf{S}_i$ in which \mathbf{S}_i is computed from the vectors pointing from the element centroids to face centroids. Detailed definitions of the above matrices can be found in Appendix C.

Based on the mimetic finite difference method, the discretized Darcy's law for the element E_i can be written in the following form (without considering the boundary conditions and at the reference conditions):

$$\mathbf{u}_i = \mathbf{M}_i^{-1} (\mathbf{e}_i^T h_{0i} - \mathbf{h}_{fi}), \quad (20)$$

where \mathbf{u}_i and \mathbf{h}_{fi} are the vectors of the total discharges and the hydraulic heads on the element faces, and h_{0i} is the hydraulic head in the center of the elements (Fig. 1b). Thus, the matrix \mathbf{M}_i^{-1} links the total discharge to the hydraulic head gradient similar to standard finite differences.

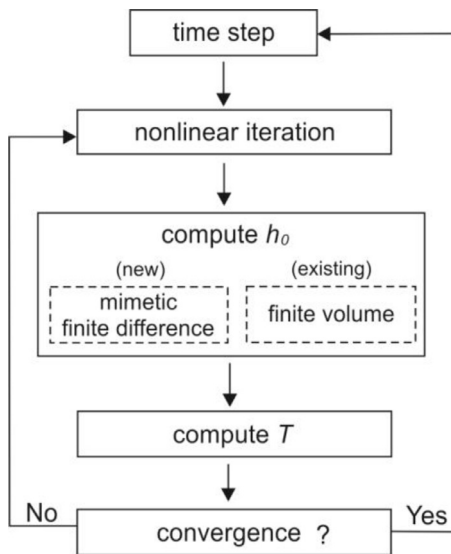


Fig. 2. Flow chart of the implementation of the mimetic finite difference method in SHEMAT-Suite.

3. Implementation

Since SHEMAT-Suite is a modular program, it is convenient to use the existing routines and to add a module for discretizing the flow equation by the mimetic finite difference method. As assembling the matrices in Eq. (18) is straightforward, the mimetic finite difference method can be easily implemented. The flow chart of the routine is shown in Fig. 2. One can choose the mimetic finite difference method or the finite volume method (two-point flux approximation) for computing the hydraulic constant density reference head. The flow equation and the heat transport equation are solved sequentially.

Similar to the existing finite volume method, the Dirichlet and Neumann boundaries and sources or sinks can be defined in the mimetic finite difference method. We can set the Dirichlet boundaries by assigning \mathbf{g}^D and reducing rows in \mathbf{D} which correspond to the element faces with the Dirichlet boundary conditions. For the Neumann boundaries, we can simply assign the total discharge values in \mathbf{g}^N . In contrast to the finite volume method, where the hydraulic constant density reference head in the Dirichlet boundary is defined in the centroid of the element, for the mimetic finite difference method it is defined on the element faces.

The linear system resulting from Eq. (19) is much larger than that of the finite volume method. As \mathbf{M}_i is positive-definite (Lie et al., 2012), the block diagonal matrix \mathbf{M} can be inverted. Schur-complement reduction, which results from a block Gaussian elimination (Zhang, 2006), can be used with respect to \mathbf{M} to eliminate \mathbf{u} (Maryška et al., 2000). Further, a similar approach can be used for eliminating \mathbf{h}_0^n . Thus, solving Eq. (19) can be simplified by solving a linear system with the variable \mathbf{h}_f^n and using \mathbf{h}_f^n for computing sequentially \mathbf{h}_0^n and \mathbf{u} . Please see the solving process based on Schur-complement reduction in Appendix D. Currently, the system is computed with the direct solver from the LAPACK library (Anderson et al., 1999).

4. Verification and benchmarking

SHEMAT-Suite-mFD was verified first against the analytical pumping test solutions in anisotropic aquifers (Papadopoulos, 1965). Both a diagonal and a symmetric full permeability tensor were considered. Three benchmarks are investigated: the first one is a case of a borehole heat exchanger in which the flow and temper-

Table 1
Properties for the numerical solution of the pumping test.

	Properties	Value
Fluid	density/ kg · m ⁻³	998
	viscosity/ Pa · s	1 × 10 ⁻³
	compressibility/ Pa ⁻¹	4.5 × 10 ⁻¹⁰
Rock	Porosity/ —	0.25
	permeability k_{xx}/m^2	3 × 10 ⁻¹²
	permeability k_{yy}/m^2	1.5 × 10 ⁻¹²
	compressibility/ Pa ⁻¹	2 × 10 ⁻⁷
	aquifer thickness/m	1
	Pumping rate/ m ³ · s ⁻¹	0.005
	Gravity/ m · s ⁻²	9.8

ature fields are coupled via variable fluid and rock properties in a homogeneous and in a highly heterogeneous permeability field. The second benchmark is a three-dimensional pumping case in a three-layer reservoir with vertically anisotropic permeability in each layer. The results of both benchmarks were compared to those obtained with SHEMAT-Suite based on the finite volume method (two-point flux approximation). The third benchmark is a fractured porous medium in which the upscaled equivalent permeability has a full tensor form. In this benchmark, results were compared with the multi-point flux approximation method (MRST, Lie et al., 2012).

4.1. Verification against the analytical pumping test solution

In this section, we verify the mimetic finite difference method for both a diagonal and a full permeability tensor against the analytical pumping test solutions in anisotropic aquifers (Papadopoulos, 1965). The problem assumes two-dimensional radial flow to a well in an infinite, homogeneous aquifer. In a confined aquifer, which is constantly pumped, the drawdown of the hydraulic head, s , is a function of pumping flow rate Q , components of aquifer transmissivity tensor \mathbf{T} , and well function $W(u_{xy})$:

$$s = \frac{Q}{4\pi\sqrt{T_{xx}T_{yy} - T_{xy}^2}} W(u_{xy}), \quad (21)$$

where $W(u_{xy})$ is expressed as:

$$W(u_{xy}) = \int_{u_{xy}}^{\infty} \frac{e^{-x}}{x} dx, \quad (22)$$

and u_{xy} is a function of coordinates of an observation point (x, y) , pumping time t , aquifer storativity S and components of aquifer transmissivity tensor \mathbf{T} :

$$u_{xy} = \frac{S(T_{xx}y^2 + T_{yy}x^2 - 2T_{xy}xy)}{4t(T_{xx}T_{yy} - T_{xy}^2)}. \quad (23)$$

First, we consider an aquifer for which the permeability tensor is diagonal. The parameters of the model are given in Table 1. A numerical model of size 21 m × 21 m × 1 m comprises 441 elements of dimension 1 m × 1 m × 1 m. The pumping well is located at the center of the domain. The simulation extends over 1000 s with a constant time step of 2 s.

The analytical solution of the drawdown of the hydraulic head at 1000 s is shown in Fig. 3a. The drawdown of hydraulic head is monitored at two points, A (3 m, 0 m) and B (0 m, 3 m). Fig. 3b shows hydraulic head vs. time calculated numerically at the two monitoring points in good agreement with the analytical solution. At monitoring point A in Fig. 3b and Fig. 4, there is a larger difference between the analytical and numerical solutions. We note that the analytical solution assumes an infinite aquifer in which the boundaries have no effect on the solution. However, in the numerical model, the area of the model is finite with constant

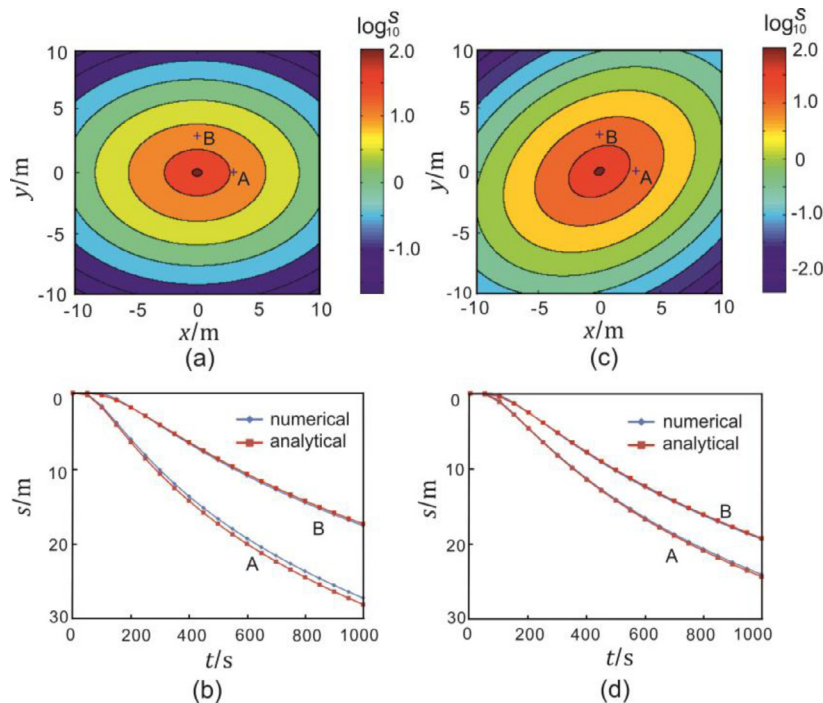


Fig. 3. Maps of the analytical drawdown of the hydraulic head, s , at the monitoring points A and B: (a) diagonal permeability tensor and (c) full permeability tensor; (b) and (d) analytical compared with the numerical solutions obtained with SHEMAT-Suite-mFD at the two monitoring points A and B. (For interpretation of the references to color in this figure legend, the reader is referred to the web version of this article.)

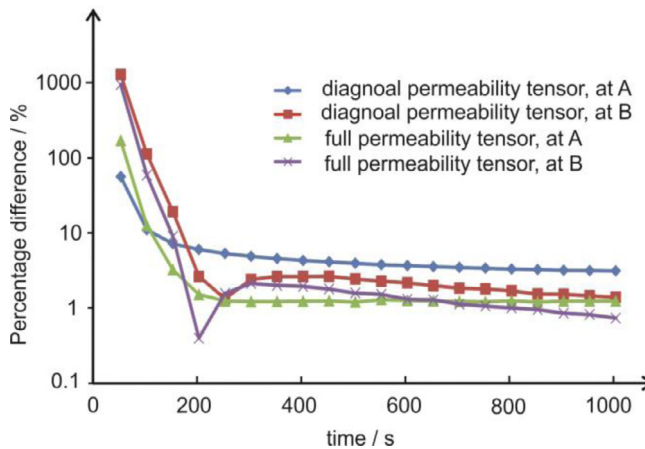


Fig. 4. Percentage difference between the numerical and analytical solutions at the two monitoring points A and B for both diagonal and full permeability tensor fields.

hydraulic head boundaries. Therefore, the boundary effect will influence the drawdown of the hydraulic head in the numerical model. As point A is located in the direction of the permeability tensor ellipse's major axis and since the drawdown is largest in the x -direction (Fig. 3b), point A is more influenced by this boundary effect.

In cases where the main directions of the permeability tensor ellipse are not aligned with the coordinate axes the permeability tensor will be symmetric and full. The corresponding tensor was computed by a rotation of 30° of the main directions of the permeability tensor ellipse (Table 2).

The analytical solution for the rotated permeability tensor can also be computed by Eq. (21). With the same boundary conditions and properties as in the first case except for permeability, the analytical solution for drawdown and comparisons between the numerical and analytical results are shown in Fig. 3c and d, respec-

Table 2

Permeability tensor components for different azimuths with respect to the coordinate system.

Azimuth/ $^\circ$	Permeability/ 10^{-12}m^2			
	k_{xx}	k_{xy}	k_{yx}	k_{yy}
0	3.0	0	0	1.5
30	2.63	0.65	0.65	1.88

tively. Again, the numerical results obtained by SHEMAT-Suite-mFD agree well with the analytical ones. Comparing the percentage difference, $\frac{|s_{\text{num}} - s_{\text{ana}}|}{s_{\text{ana}}} \times 100\%$, between the numerical solution, s_{num} , and analytical solution, s_{ana} (Fig. 4) shows differences below 10%, in general. Large differences, exceeding $10^3\%$, occur at the beginning of pumping. Since s is small at early times, even a small absolute difference between numerical and analytical solutions result in a large percentage difference.

4.2. Borehole heat exchanger

A steady state borehole heat exchanger model was defined for testing the coupling between flow and heat transport in SHEMAT-Suite-mFD in a horizontally anisotropic permeability model with variable fluid and rock properties. A $30 \text{ m} \times 15 \text{ m} \times 1 \text{ m}$ domain is discretized into $450 \text{ 1 m} \times 1 \text{ m} \times 1 \text{ m}$ Cartesian grid blocks. In the simulation, fluid and rock properties varied with pressure and temperature as generated by the equations of state implemented in SHEMAT-Suite (Clauser, 2003). The corresponding constant rock properties are shown in Table 3.

The initial temperature of the model is 10°C . A heat exchanger with a heat production rate of $H = -0.5 \text{ W/m}^3$ is placed in the left part of the model. The temperature at the four boundaries is held constant at 10°C . Fluid flow from left to right results from constant hydraulic heads, h_0 , at the two lateral boundaries

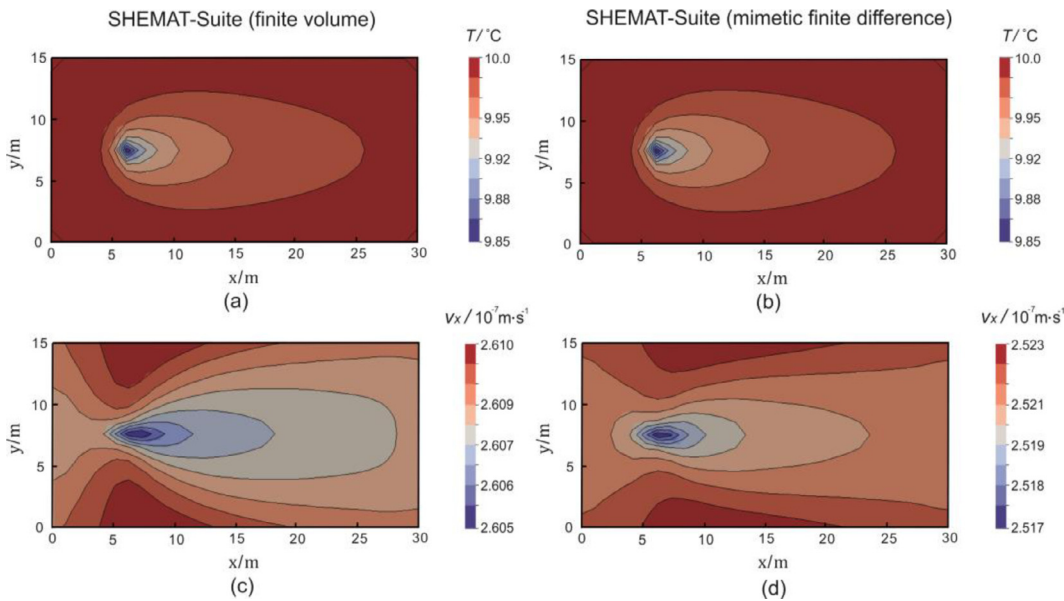


Fig. 5. Temperature, T , contour plots calculated with (a) SHEMAT-Suite (finite volume method) and (b) SHEMAT-Suite-mFD, and specific discharge in the x -direction, v_x , contour plots calculated with (c) SHEMAT-Suite (finite volume method) and (d) SHEMAT-Suite-mFD.

Table 3
Constant rock properties used in the borehole heat exchanger problem.

Rock property	Value
Porosity/ –	0.37
Permeability k_{xx}/m^2	1×10^{-12}
Permeability k_{yy}/m^2	1.5×10^{-12}
Compressibility/ Pa^{-1}	1×10^{-10}
Volumetric thermal capacity/ $\text{J} \cdot \text{m}^{-3} \cdot \text{K}^{-1}$	2.9×10^6

of 101 m and 100 m, respectively. No-flow conditions apply at the other boundaries.

Fig. 5a and b show temperature contours corresponding to solutions using SHEMAT-Suite (finite volume method) and SHEMAT-Suite-mFD, respectively. As can be expected the temperature fields are distorted by the flow direction to the right. While, the temperature contours agree well between the two methods (Fig. 5a and b), the specific discharge in the x -direction shows larger differences of up to 4% (Figs. 5c, d, and 6).

As the fluid properties are influenced by the temperature and the pressure, the distribution of specific discharge within the model is not uniform (Fig. 5c and d). The variations of specific discharge around the heat exchanger are similar between the two methods, although the specific discharge computed by SHEMAT-Suite (finite volume method) is somewhat larger than that by SHEMAT-Suite-mFD (Fig. 5c and d). This may be attributed to the location where the Dirichlet boundary condition is defined: the finite volume method defines it at the centroid of the element, the mimetic finite difference method on the faces of the element. Accordingly, for the finite volume method, the slightly shorter distance between the Dirichlet boundaries results in a higher specific discharge in the entire domain. The percentage difference between the two methods is below 4% (Fig. 6c and d) with a maximum at the heat exchanger where the temperature gradient is largest. However, such differences will decrease with the number of elements used. Their influence on the temperature can be neglected, the percentage difference in temperature being below 0.05% in this model.

The above results are based on a homogeneous anisotropic model. We also solved a flow and heat transport problem for a highly heterogeneous model. The permeability of the cells in the model (Fig. 6a) is upscaled from 486,000 cells from the SPE-10 model. The contrast of the upscaled permeability is close to two orders of magnitude. The model dimensions and other parameters are the same as in the homogeneous model.

The same flow and heat transport problem was solved by both using SHEMAT-Suite and SHEMAT-Suite-mFD. The specific discharge in the x -direction computed by SHEMAT-Suite-mFD is shown in Fig. 6b. Compared to the homogeneous model, the specific discharge is highly influenced by the heterogeneity of the permeability field. And the effects of variable fluid properties on the specific discharge will no longer be obvious as in the homogeneous model. The percentage differences of the specific discharge increase compared to that in the homogeneous model (Fig. 7c and d). However, they are below 12%, which indicates the consistency of the results between the two methods.

This benchmark shows that SHEMAT-Suite-mFD captures the coupling well between flow and heat transfer in the horizontally anisotropic permeability model and is also applicable in the highly heterogeneous and anisotropic permeability model.

4.3. Pumped multiple-layer reservoir

As a third benchmark, we use a pumped multiple-layer model for demonstrating three-dimensional performance of the mimetic finite difference scheme. The size of a confined aquifer model is assumed to be $15 \text{ m} \times 15 \text{ m} \times 3 \text{ m}$, discretized into a uniform $1 \text{ m} \times 1 \text{ m} \times 1 \text{ m}$ Cartesian grid (Fig. 8). The model consists of three layers with vertically anisotropic permeability. The fluid and rock properties of each layer are shown in Table 4.

We assume fluid flowing from the front ($y = 0 \text{ m}$) to the rear ($y = 15 \text{ m}$) according to two constant hydraulic heads of 101 m and 100 m, at these boundaries, respectively. The other boundaries are no-flow boundaries. A pumping well is located at the central layer with a flow rate $Q = -0.01 \text{ m}^3/\text{s}$. The duration of pumping is 3000 s and the time step in numerical model is 10 s.

A monitoring point is located at a depth of 1.5 m (Fig. 8). The hydraulic head drawdown and the changes of the specific discharge

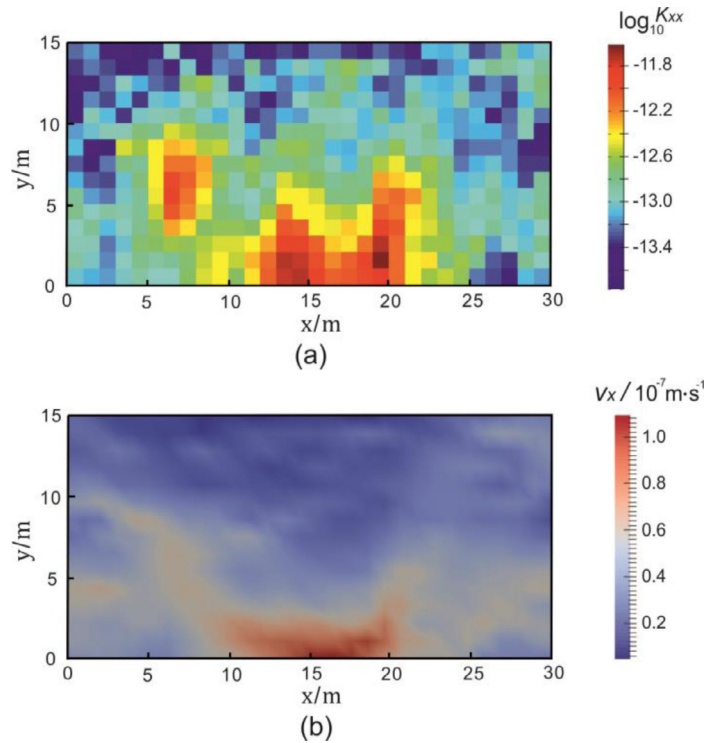


Fig. 6. (a) Permeability in the x -direction, k_{xx} , and (b) specific discharge in the x -direction, v_x , calculated by SHEMAT-Suite-mFD in the heterogeneous model.

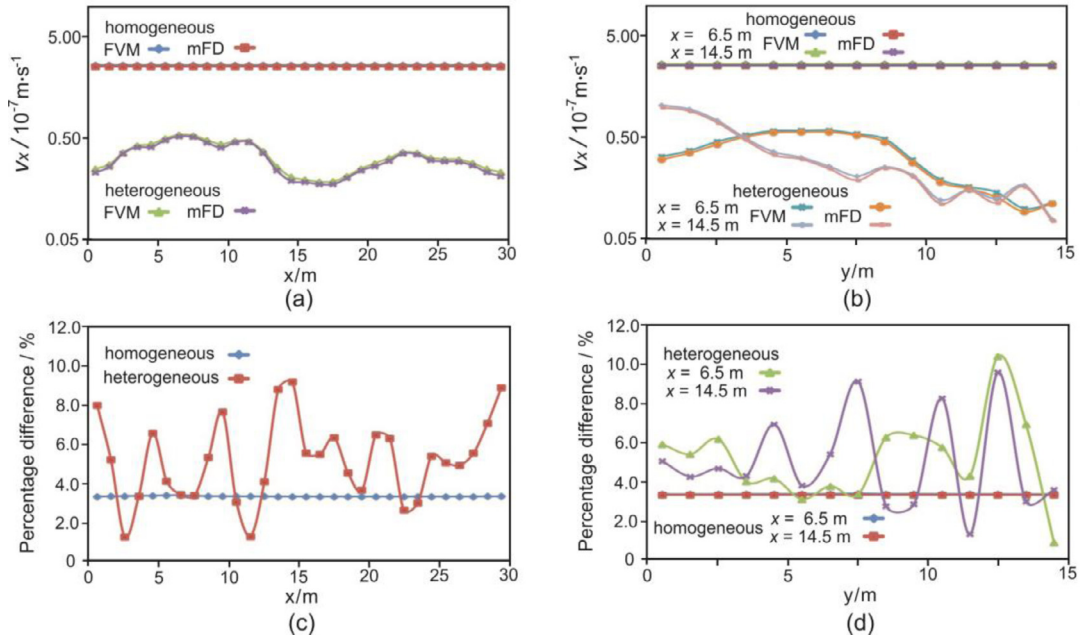


Fig. 7. Specific discharge in the x -direction, v_x , along (a) $y = 7.5 \text{ m}$ and (b) $x = 6.5 \text{ m}$ and $x = 14.5 \text{ m}$ with SHEMAT-Suite (finite volume method) and SHEMAT-Suite-mFD and the percentage difference of the temperature between the two methods along (c) $y = 7.5 \text{ m}$ and (d) $x = 6.5 \text{ m}$ and $x = 14.5 \text{ m}$ for both the homogeneous and heterogeneous models.

at the monitoring point are shown in Fig. 9. The hydraulic head drawdown and the specific discharge in the x -direction computed by SHEMAT-Suite (finite volume method) are both larger than those values computed by SHEMAT-Suite-mFD. The percentage differences of the hydraulic head and the specific discharge in the x -direction, v_x , between the two methods, $\frac{|h_{\text{mFD}} - h_{\text{FVM}}|}{h_{\text{FVM}}} \times 100 \%$ and $\frac{|v_{x\text{mFD}} - v_{x\text{FVM}}|}{v_{x\text{FVM}}} \times 100 \%$, tend to steady at 4% and 20%, respectively (Fig. 9a and b).

In case the principle directions of the permeability tensor ellipsoid are not aligned with the coordinates, the permeability will have a symmetric tensor form, e.g., due to the existence of a set of inclined fractures. We thus assume the components of the permeability tensor, k_{xz} and k_{yz} , in the top and bottom layers have positive values of $1.0 \times 10^{-13} \text{ m}^2$ rather than zero. Except for the difference in permeability, we use the same model and solve the same flow problem as in the previous model.

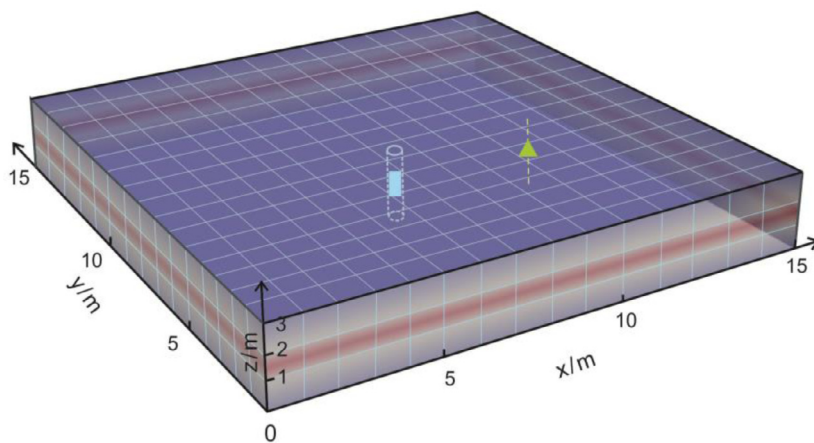


Fig. 8. The three-dimensional Cartesian grids of the pumped multiple-layer model. The blue cylinder indicates the pumping well. The green triangle denotes the monitoring point at the depth of 1.5 m in the central, high-permeability layer. (For interpretation of the references to color in this figure legend, the reader is referred to the web version of this article.)

Table 4
Properties of the pumped multiple-layer reservoir model.

Properties		Value		
Fluid	density/ kg · m ⁻³	998		
	viscosity/ Pa · s	8.9×10^{-4}		
	compressibility/ Pa ⁻¹	4.6×10^{-10}		
Rock		Bottom layer	Central layer	Top layer
	porosity/ –	0.1	0.12	0.1
	permeability k_{xx}/m^2	7.5×10^{-13}	15×10^{-13}	7.5×10^{-13}
	permeability k_{yy}/m^2	7.5×10^{-13}	15×10^{-13}	7.5×10^{-13}
	permeability k_{zz}/m^2	2.0×10^{-13}	3.0×10^{-13}	2.0×10^{-13}
	compressibility/ Pa ⁻¹	5×10^{-7}	5×10^{-7}	5×10^{-7}

It shows that for the hydraulic head and the specific discharge in the x -direction, the results of using the diagonal and the symmetric permeability tensor are nearly consistent by SHEMAT-Suite-mFD (Fig. 9a and b). However, during pumping, the specific discharge in the z -direction increases when using the full permeability tensor whereas it keeps as zero when neglecting the off-diagonal terms. It turns out that SHEMAT-Suite-mFD can model interface changes accurately when anisotropy is not aligned with the coordinate axes, whereas such effect cannot be observed by SHEMAT-Suite where only the diagonal permeability tensor could be used.

4.4. Modeling fractured porous medium

In this benchmark, we use SHEMAT-Suite-mFD for modeling flow through a two-dimensional, fractured porous medium and compare the results with those obtained by the multi-point flux approximation method (MRST, Lie et al., 2012) and by the finite volume method (SHEMAT-Suite). The fracture network pattern is adopted from Lee et al. (2001) (Fig. 10a). We assume a fracture aperture of $3 \mu\text{m}$ and a matrix permeability k_m of 1 nm^2 . According to the cubic law, the permeability of each fracture, k_f , is $7.5 \times 10^5 \text{ nm}^2$.

We constructed an equivalent fracture model (EFM) for this fractured porous medium. The fracture domain is discretized into a $2 \text{ m} \times 2 \text{ m}$ Cartesian grid. The equivalent permeability tensor of each element is computed according to the multi-boundary fracture upscaling method (Chen et al., 2015) based on the discrete fracture simulator developed by Sandve et al. (2012).

Then, we solved a steady-state flow problem for this equivalent fracture model. At the left and right boundaries, constant pres-

sures are held at 20 Pa and 0 Pa , respectively. There is no flow at the front and rear boundaries, the pressure decreases linearly from left to right. The pressure fields computed by the finite volume method (SHEMAT-Suite), by the multi-point flux approximation method (MRST), and by the mimetic finite difference method (SHEMAT-Suite-mFD) are shown in Fig. 10b, row 1, column 2–4. Further, the equivalent permeability tensor computed by the multi-boundary fracture upscaling method (Chen et al., 2015) may not be symmetric before averaging the off-diagonal terms. We also used the asymmetric permeability tensor directly to solve the flow problem by applying the mimetic finite difference method (SHEMAT-Suite-mFD, Fig. 10b, row 1, column 5).

We compared pressures and flow rates in the x -direction of these equivalent fracture models with those of the discrete fracture model (DFM). The pressure on unstructured grids in the discrete fracture model (DFM) is averaged on a $2 \text{ m} \times 2 \text{ m}$ Cartesian grid as in the equivalent fracture model (Fig. 10b, column 1).

The percentage differences of the pressure between the equivalent fracture models (EFM) and the averaged discrete fracture model (DFM), $\frac{|p_{\text{EFM}} - p_{\text{DFM}}|}{p_{\text{DFM}}} \times 100 \%$, are shown in Fig. 10b, row 2. There is a higher difference in the right part of the model where the pressure is lower. The difference between the models based on the diagonal permeability tensor and the full permeability tensors are obvious. However, the similarities of differences between the equivalent fracture models based on the full permeability tensors indicate the good consistency of the results computed by the multi-point flux approximation (MRST) and the mimetic finite difference method (SHEMAT-Suite-mFD).

Table 5 summarizes the flow rates in the x -direction, q_x , for the four equivalent fracture models. It turns out that the differences in flow rate between SHEMAT-Suite-mFD and the multi-point flux approximation method (MRST) are below 10 %. The differences in flow rate between the equivalent models based on the symmetric and asymmetric permeability tensors are negligible. However, when using the diagonal permeability tensor, i.e., neglecting the off-diagonal terms, larger differences arise.

The accuracies of numerical methods may be influenced by the anisotropy of the equivalent permeability of the model. The equivalent permeability becomes more anisotropic as the difference in permeability between the rock matrix and the fractures increases. To this end, we use a lower rock matrix permeability k_m of 0.1 nm^2 and further of 0.01 nm^2 and conduct similar analyses as above. The results are shown in Fig. 10b row 3–6 and in Table 5.

Table 5

The flow rates in the x -direction, q_x , and the oscillating ratios, R by using different schemes or different fracture models.

	Anisotropy	Discrete fracture model	Equivalent fracture model		
			MPFA	diagonal tensor	symmetric tensor
			FVM	MPFA	mFD
Low	$q_x / 10^{-14} \text{ m}^3/\text{s}$	3.75	5.50	3.95	4.27
	$R/\%$	0	0	0	0
Medium	$q_x / 10^{-14} \text{ m}^3/\text{s}$	1.81	2.98	0.69	1.54
	$R/\%$	0	0	20	1
High	$q_x / 10^{-14} \text{ m}^3/\text{s}$	1.36	2.55	0.54	0.65
	$R/\%$	0	0	8	7
					0.73
					5

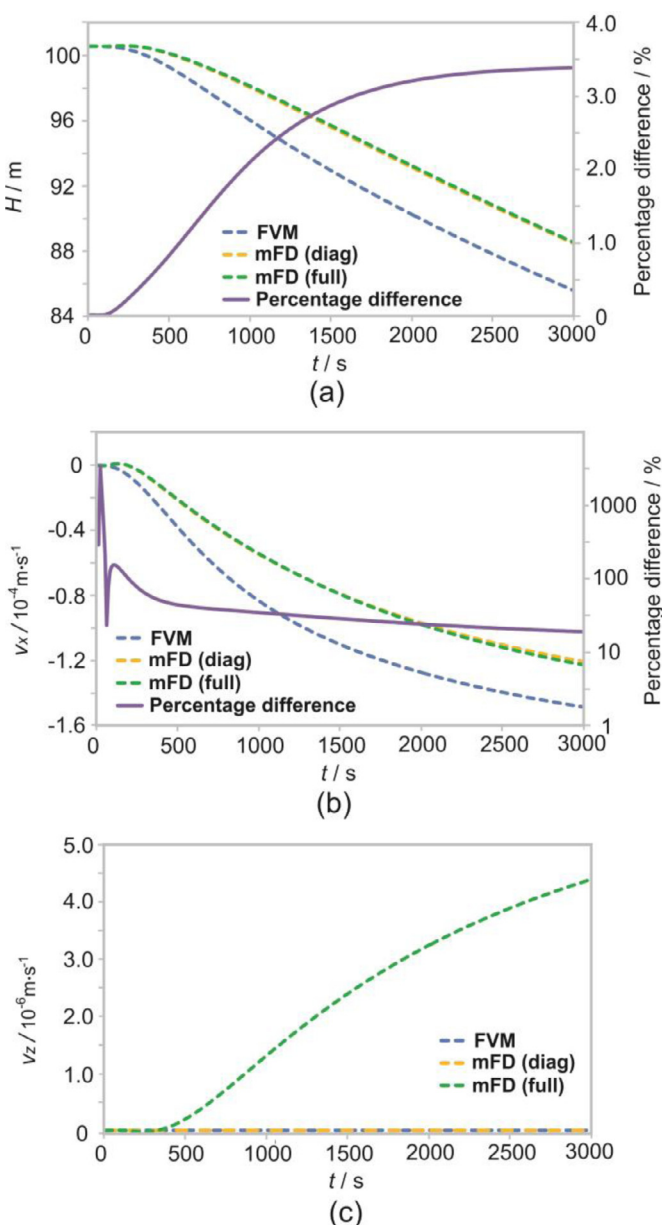


Fig. 9. (a) The drawdowns of the hydraulic head and the percentage differences, (b) the specific discharge in the x -direction, v_x , and the percentage differences, and (c) the specific discharge in the z -direction, v_z , computed by SHEMAT-Suite (finite volume method), SHEMAT-Suite-mFD (diag) and SHEMAT-Suite-mFD (full) at the monitoring point.

Compared to the former, less anisotropic model, the percentage differences in both pressure and flow rate show an increasing trend in the equivalent fracture models (Fig. 11). Further, the oscillating (non-monotonic) solutions, i.e., pressures are out of the range of the boundary values, arise in the models with higher anisotropy and increase with the anisotropy when using the full permeability tensor, and the oscillating ratio, R , the percentage of elements with oscillating solutions, is larger when using the multi-point flux approximation method (MRST) than using the mimetic finite difference method. In contrast, pressure computed by the finite volume method remains monotonic in all the anisotropic models. In the models with higher anisotropy, when comparing the difference between using the symmetric and asymmetric permeability tensor, slightly lower percentage differences of pressure are observed for the asymmetric permeability tensor (Fig. 11).

The more non-monotonic solutions result in larger errors both in pressure and flow rate when using the full permeability tensor (Table 5). In Fig. 11, it is shown that the percentage differences increase gradually with the anisotropy when using the mimetic finite difference method, whereas the increase is fluctuant when using the multi-point flux approximation method (MRST). For highly anisotropic models, the flow rate calculated by the former has a smaller error than that computed by the latter. This indicates that the solutions calculated by the mimetic finite difference method are more stable and more accurate than that by the multi-point flux approximation method (MRST) for highly anisotropic models. It may be due to the fact that the mimetic finite difference method is unconditionally coercive which ensures the stability and convergence of the solutions, whereas the multi-point flux approximation method, in which an element face contains more than one total discharge unknown (e.g., Aavatsmark et al., 1996), is conditionally coercive (Droniou, 2014). When using the finite volume method, although the errors in pressure are lower than using the other two methods, it produces large errors in flow rate even in the lowly anisotropic models.

5. Summary

The mimetic finite difference method was implemented for discretizing the flow equation in the flow and heat transport simulator SHEMAT-Suite. The scheme can model anisotropic flow with full permeability tensors resulting from upscaling of a fine-grid geostatistical model or a fractured rock model, laboratory experiments (Renard et al., 2001), and field measurements (Hsieh and Neuman, 1985; Neupauer et al., 2006). Thus, two options are available within the SHEMAT-Suite framework for modeling flow in specific geological systems, the finite volume method and the mimetic finite difference method, which may be chosen according to the complexity of the model. Further, the hydraulic head and the total discharge are solved simultaneously when using the mimetic finite difference method. This will reduce the errors of the specific discharge compared to the finite volume method or the classical

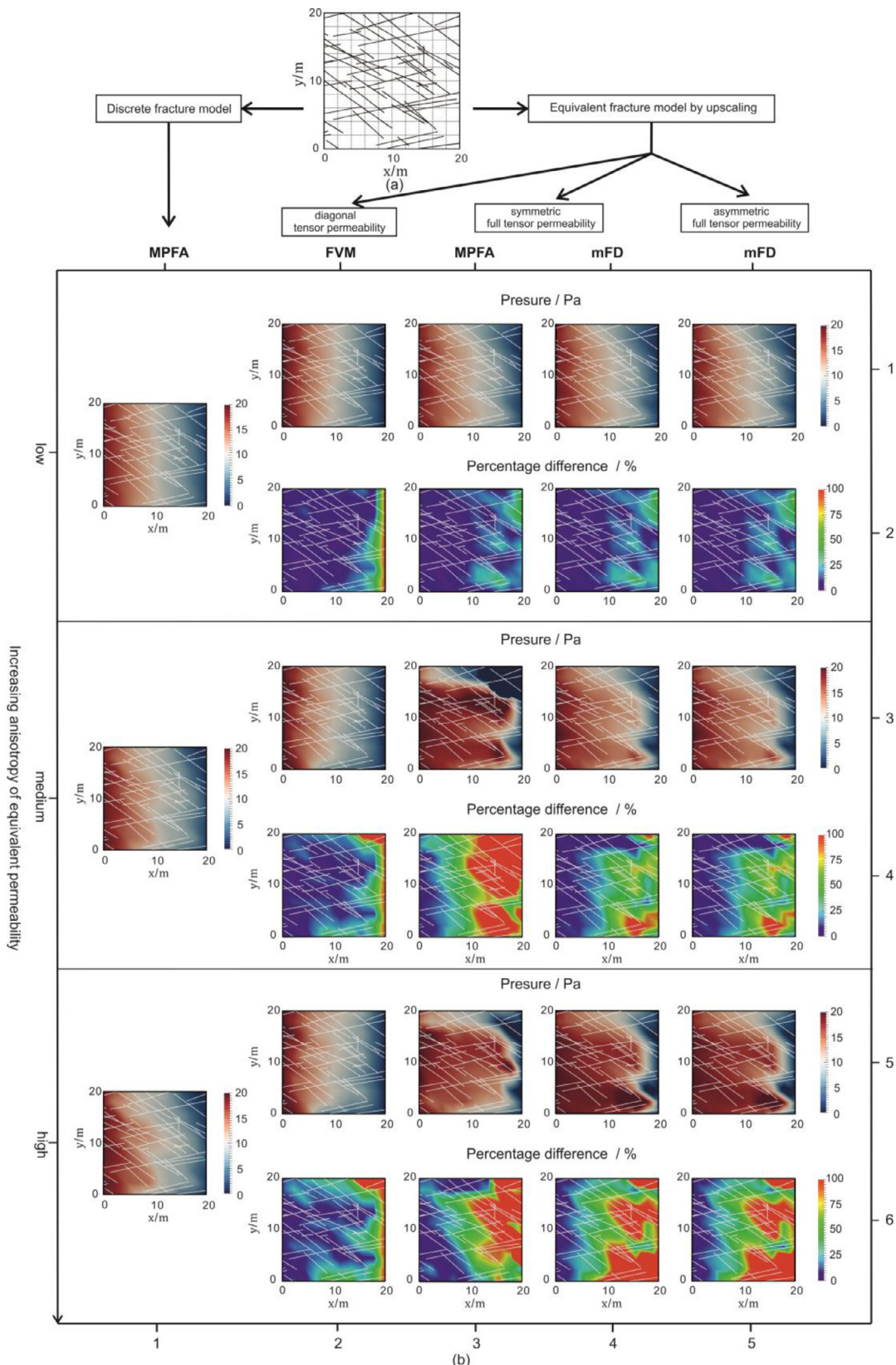


Fig. 10. (a) Fracture pattern and Cartesian $2\text{ m} \times 2\text{ m}$ grids. (b) Pressure fields of the averaged discrete fracture model, column 1, and of the equivalent fracture models, row 1 ($k_m = 1\text{ nm}^2$), row 3 ($k_m = 0.1\text{ nm}^2$), and row 5 ($k_m = 0.01\text{ nm}^2$), and their percentage differences, row 2, row 4, and row 6. The white lines in (b) denote the fractures. (For interpretation of the references to color in this figure legend, the reader is referred to the web version of this article.)

Table 6
The size of linear equations for different methods in the models.

Model	The number of cells	The number of unknowns in the linear equation			
		DFM (MPFA)	FVM	MPFA	mFD
Pumping test	441	–	–	–	1722
Borehole heat exchanger	450	–	450	–	1815
Pumped multiple-layer	675	–	675	–	2250
Fractured porous medium	100	3086	100	140	380

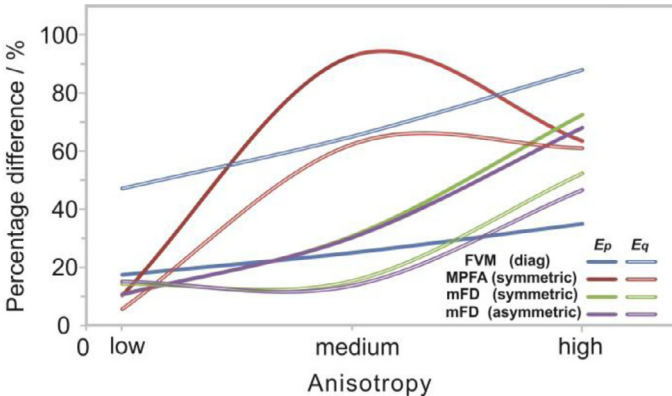


Fig. 11. The changes of the percentage differences of pressure and flow rate in the x -direction, q_x , between the equivalent fracture models and the discrete fracture models, E_p and E_q , with the anisotropy of the model.

finite element method. Additionally, the method is locally conservative as the finite volume method, which is beneficial when modeling flow problems.

At the same time, the computation effort increases when using the mimetic finite difference method. For a Cartesian grid system, the number of unknowns of the linear system solved by the finite volume method (two-point flux approximation) equals the number of elements, while for the mimetic finite difference method it is the number of element faces. Thus, the scale of the linear system to be solved is about three times larger than that of the finite volume method (two-point flux approximation). The sizes of linear equations in all the models are summarized in Table 6. Accordingly, parallelization of the new scheme will be required for efficiently computing large-scale field reservoir models. However, compared to using the discrete fracture models, using the equivalent fracture models computed by the mimetic finite difference method is worthwhile as it reduces the computational effort as well as preserves better accuracy than that by the other two methods.

Based on the concept of the representative elementary volume (REV), the anisotropy in permeability is often represented by a diagonal or symmetric tensor. However, it has been observed that permeability, the anisotropy of the permeability, and the existence of an REV may change with spatial scales (Clauer, 1992; Zijl, 1999; Zhang et al., 2000). Also, the permeability tensor may not be inherently symmetric before averaging the off-diagonal terms during upscaling (e.g., Zijl, 1996). Using flow-based fracture upscaling, the permeability tensor is related to fracture geometry and boundary conditions for flow simulations. For periodic boundary conditions, the upscaled permeability tensor always has a symmetric (including diagonal) form (e.g., Koudina et al., 1998). However, for linear boundary conditions, which are closer to the natural flow state than the former, the form of the permeability tensor will depend on the fracture distribution (e.g., Chen et al., 2015, Fig. 12). In such cases also an asymmetric permeability tensor may arise. This will

require numerical methods which can handle different forms of highly anisotropic permeability accurately.

The percentage difference between equivalent fracture models and discrete fracture models relates mainly to the accuracies of the upscaling procedure and the numerical schemes used for the equivalent fracture model. When using a highly anisotropic model, the percentage differences increase in all of the equivalent fracture models. Neglecting the influence of the upscaling procedure in models based on a diagonal permeability tensor, large differences may occur due to neglecting the off-diagonal terms of the permeability tensor. For the full permeability tensor, differences may occur due to the instability of the schemes. Even though the superiority of using the asymmetric permeability tensor over using the symmetric permeability tensor could be negligible in the fractured porous medium models, the application of the mimetic finite difference method enables the direct use of asymmetric permeability tensors in numerical models.

Coupling between the flow equation and the heat transport equation shows the potential for applying the mimetic finite difference method in modeling fractured geothermal reservoirs with a full equivalent permeability tensor. Further, the scheme can also be applied for coupling flow and chemical transport or for multiphase non-isothermal flow in which the full permeability tensor is crucial. The simple implementation of the mimetic finite difference method makes it useful for any existing finite difference or finite volume simulator. In the near future, the module of the mimetic finite difference discretization (mFD) written in Fortran will be released under the GPL open source license and can be obtained from the author.

6. Conclusions

We discretized the flow equation in the hydrothermal simulator SHEMAT-Suite by using the mimetic finite difference method and coupled it with the heat transport equation.

- (1) The implementation of the mimetic finite difference method is relatively simple. It can be incorporated into any existing finite difference or finite volume simulator.
- (2) The results obtained by SHEMAT-Suite-mFD agree well with the analytical solution and with those obtained by other schemes, namely the finite volume method (two-point flux approximation, SHEMAT-Suite) for the diagonal permeability tensor and the multi-point flux approximation method (MRST) for the symmetric full permeability tensor. Further, the mimetic finite difference yields better results for highly anisotropic equivalent fracture models than the multi-point flux approximation method (MRST).
- (3) The new implementation yields accurate results also in case of coupled flow and heat transport with variable fluid and rock properties in both the homogeneous and highly heterogeneous models.
- (4) Results for an asymmetric full permeability tensor were compared with those for a symmetric full permeability tensor. The improvement obtained by using the former compared to the latter is slight for the equivalent fracture models.

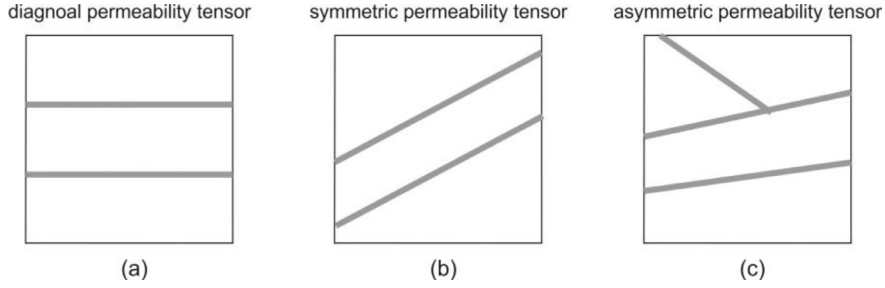


Fig. 12. Fracture distributions and the corresponding forms of the equivalent permeability tensors. The black rectangles denote the elements and the bold gray lines denote fractures.

- (5) The percentage differences of pressure and flow rate between the equivalent fracture model and the discrete fracture model increase with the anisotropy of the equivalent permeability.

Acknowledgments

This work was funded by the China Scholarship Council - RWTH Aachen University Joint PhD Program. We thank the editor and three anonymous reviewers for carefully reading and for very helpful comments to improve the manuscript.

Appendix A

We introduce the following bilinear forms:

$$b(\mathbf{w}, \mathbf{v}) = \sum_{E \in \Omega_h} \int_E \mathbf{w} \cdot \frac{\mu}{\rho_f g} \mathbf{k}^{-1} \mathbf{v} dE, \quad (\text{A1})$$

$$c(\mathbf{w}, h_0^n) = \sum_{E \in \Omega_h} \int_E h_0^n \cdot \nabla \cdot \mathbf{w} dE, \quad (\text{A2})$$

$$c(\mathbf{v}, \varphi) = \sum_{E \in \Omega_h} \int_E \nabla \cdot \mathbf{v} \varphi dE, \quad (\text{A3})$$

$$j(\varphi, h_0^n) = \sum_{E \in \Omega_h} \int_E \varphi S_s \frac{h_0^n}{\Delta t} dE, \quad (\text{A4})$$

$$(\nabla \cdot \mathbf{w}, \rho_r z) = \sum_{E \in \Omega_h} \int_E \rho_r z \cdot \nabla \cdot \mathbf{w} dE, \quad (\text{A5})$$

$$(h_0 + \rho_r z, \mathbf{w} \cdot \mathbf{n}) = \sum_{E \in \Omega_h} \int_{S_E} (h_0 + \rho_r z) \mathbf{w} \cdot \mathbf{n} ds_E, \quad (\text{A6})$$

$$(\varphi, Q) = \sum_{E \in \Omega_h} \int_E \varphi Q dE, \quad (\text{A7})$$

$$\left(\varphi, S_s \frac{h_0^{n-1}}{\Delta t} \right) = \sum_{E \in \Omega_h} \int_E \varphi S_s \frac{h_0^{n-1}}{\Delta t} dE, \quad (\text{A8})$$

$$d(\mathbf{w}, h_f^n) = \sum_{E \in \Omega_h} \int_{S_E} h_f^n \mathbf{w} \cdot \mathbf{n}_E ds_E, \quad (\text{A9})$$

$$d(\mathbf{v}, \eta) = \sum_{E \in \Omega_h} \int_{S_E} \eta \mathbf{v} \cdot \mathbf{n}_E ds_E, \quad (\text{A10})$$

$$(g^N, \eta) = \sum_{E \in \Omega_h} \int_{S_E} \eta g^N ds_E, \quad (\text{A11})$$

where S_E is the perimeter of the element E , \mathbf{n}_E is the outward normal unit vector orthogonal to the face of the element E , η is a scalar valued function, g^N is the value of Neumann boundary.

Appendix B

Let $F_k^{(i)}$ be the k -th face of the element E_i , we use a slight modified version of the lowest-order Raviart-Thomas-Nédélec space for V (Arbogast et al., 1995; Droniou, 2014):

$$V = \text{span} \left\{ \omega_k^{(i)}, i = 1, 2, \dots N_E, k = 1, 2, \dots 6 \right\}, \omega_i(x) = \begin{cases} 1, & \text{if } x \in F_k^{(i)}, \\ 0, & \text{otherwise.} \end{cases} \quad (\text{B1})$$

The approximate subspace U consists of constant basis functions:

$$U = \text{span} \{ \varphi_i, i = 1, 2, \dots N_E \}, \varphi_i(x) = \begin{cases} 1, & \text{if } x \in E_i, \\ 0, & \text{otherwise.} \end{cases} \quad (\text{B2})$$

The approximate subspace Π consists of basis functions that are constant on each element face $\gamma_j^i = \partial E_i \cap \partial E_j$:

$$\Pi = \text{span} \{ \eta_i, i = 1, 2, \dots N_E \}, \eta_i(x) = \begin{cases} 1, & \text{if } x \in \gamma_j^i, \\ 0, & \text{otherwise.} \end{cases} \quad (\text{B3})$$

Appendix C

Using the definitions by Lie et al. (2012), we have:

$$\mathbf{N}_i = \begin{bmatrix} a_1^{(i)} n_{11}^{(i)} & a_1^{(i)} n_{12}^{(i)} & a_1^{(i)} n_{13}^{(i)} \\ a_2^{(i)} n_{21}^{(i)} & a_2^{(i)} n_{22}^{(i)} & a_2^{(i)} n_{23}^{(i)} \\ a_3^{(i)} n_{31}^{(i)} & a_3^{(i)} n_{32}^{(i)} & a_3^{(i)} n_{33}^{(i)} \\ a_4^{(i)} n_{41}^{(i)} & a_4^{(i)} n_{42}^{(i)} & a_4^{(i)} n_{43}^{(i)} \\ a_5^{(i)} n_{51}^{(i)} & a_5^{(i)} n_{52}^{(i)} & a_5^{(i)} n_{53}^{(i)} \\ a_6^{(i)} n_{61}^{(i)} & a_6^{(i)} n_{62}^{(i)} & a_6^{(i)} n_{63}^{(i)} \end{bmatrix}, \quad (\text{C1})$$

where $a_j^{(i)}$, $j = 1, 2, \dots 6$, denotes the area of the face $F_j^{(i)}$ in the element E_i and $n_{jk}^{(i)}$, $k = 1, 2, 3$, is the component of the unit outward normal vector on the face $F_j^{(i)}$.

$$\mathbf{k}_i = \begin{bmatrix} k_{11}^{(i)} & k_{12}^{(i)} & k_{13}^{(i)} \\ k_{21}^{(i)} & k_{22}^{(i)} & k_{23}^{(i)} \\ k_{31}^{(i)} & k_{32}^{(i)} & k_{33}^{(i)} \end{bmatrix}, \quad (\text{C2})$$

$$\mathbf{A}_i = \begin{bmatrix} a_1^{(i)} & 0 & 0 & 0 & 0 & 0 \\ 0 & a_2^{(i)} & 0 & 0 & 0 & 0 \\ 0 & 0 & a_3^{(i)} & 0 & 0 & 0 \\ 0 & 0 & 0 & a_4^{(i)} & 0 & 0 \\ 0 & 0 & 0 & 0 & a_5^{(i)} & 0 \\ 0 & 0 & 0 & 0 & 0 & a_6^{(i)} \end{bmatrix}, \quad (C3)$$

$$\mathbf{I}_i = \begin{bmatrix} 1 & 0 & 0 & 0 & 0 & 0 \\ 0 & 1 & 0 & 0 & 0 & 0 \\ 0 & 0 & 1 & 0 & 0 & 0 \\ 0 & 0 & 0 & 1 & 0 & 0 \\ 0 & 0 & 0 & 0 & 1 & 0 \\ 0 & 0 & 0 & 0 & 0 & 1 \end{bmatrix}, \quad (C4)$$

$$\mathbf{S}_i = \begin{bmatrix} c_{11}^{(i)} - c_1^{(i)} & c_{12}^{(i)} - c_2^{(i)} & c_{13}^{(i)} - c_3^{(i)} \\ c_{21}^{(i)} - c_1^{(i)} & c_{22}^{(i)} - c_2^{(i)} & c_{23}^{(i)} - c_3^{(i)} \\ c_{31}^{(i)} - c_1^{(i)} & c_{32}^{(i)} - c_2^{(i)} & c_{33}^{(i)} - c_3^{(i)} \\ c_{41}^{(i)} - c_1^{(i)} & c_{42}^{(i)} - c_2^{(i)} & c_{43}^{(i)} - c_3^{(i)} \\ c_{51}^{(i)} - c_1^{(i)} & c_{52}^{(i)} - c_2^{(i)} & c_{53}^{(i)} - c_3^{(i)} \\ c_{61}^{(i)} - c_1^{(i)} & c_{62}^{(i)} - c_2^{(i)} & c_{63}^{(i)} - c_3^{(i)} \end{bmatrix}, \quad (C5)$$

where $c_{jk}^{(i)}$ is the coordinate of the centroid of the face $F_j^{(i)}$ in the element E_i in the x -, y -, or z -direction ($k=1, 2, 3$). $c_k^{(i)}$ is the coordinate of the centroid of the element E_i in the x -, y -, or z -direction ($j=1, 2, 3$).

$$\mathbf{Z}_i = \left(\mathbf{Z}_1^{(i)}, \mathbf{Z}_2^{(i)}, \mathbf{Z}_3^{(i)} \right)$$

$$= \begin{bmatrix} a_1^{(i)}(c_{11}^{(i)} - c_1^{(i)}) & a_1^{(i)}(c_{12}^{(i)} - c_2^{(i)}) & a_1^{(i)}(c_{13}^{(i)} - c_3^{(i)}) \\ a_2^{(i)}(c_{21}^{(i)} - c_1^{(i)}) & a_2^{(i)}(c_{22}^{(i)} - c_2^{(i)}) & a_2^{(i)}(c_{23}^{(i)} - c_3^{(i)}) \\ a_3^{(i)}(c_{31}^{(i)} - c_1^{(i)}) & a_3^{(i)}(c_{32}^{(i)} - c_2^{(i)}) & a_3^{(i)}(c_{33}^{(i)} - c_3^{(i)}) \\ a_4^{(i)}(c_{41}^{(i)} - c_1^{(i)}) & a_4^{(i)}(c_{42}^{(i)} - c_2^{(i)}) & a_4^{(i)}(c_{43}^{(i)} - c_3^{(i)}) \\ a_5^{(i)}(c_{51}^{(i)} - c_1^{(i)}) & a_5^{(i)}(c_{52}^{(i)} - c_2^{(i)}) & a_5^{(i)}(c_{53}^{(i)} - c_3^{(i)}) \\ a_6^{(i)}(c_{61}^{(i)} - c_1^{(i)}) & a_6^{(i)}(c_{62}^{(i)} - c_2^{(i)}) & a_6^{(i)}(c_{63}^{(i)} - c_3^{(i)}) \end{bmatrix}. \quad (C6)$$

For the structured hexahedral elements, the column vector of \mathbf{S}_i , $\mathbf{S}_k^{(i)}$, are orthogonal and the column vector $\mathbf{Z}_k^{(i)}$ in \mathbf{Z}_i will be orthogonal correspondingly. Accordingly, computing the orthonormal

basis \mathbf{R}_i for the matrix \mathbf{Z}_i can be simplified by:

$$\mathbf{R}_i = \begin{bmatrix} \frac{z_{11}^{(i)}}{\|\mathbf{Z}_1^{(i)}\|} & \frac{z_{12}^{(i)}}{\|\mathbf{Z}_2^{(i)}\|} & \frac{z_{13}^{(i)}}{\|\mathbf{Z}_3^{(i)}\|} \\ \frac{z_{21}^{(i)}}{\|\mathbf{Z}_1^{(i)}\|} & \frac{z_{22}^{(i)}}{\|\mathbf{Z}_2^{(i)}\|} & \frac{z_{23}^{(i)}}{\|\mathbf{Z}_3^{(i)}\|} \\ \frac{z_{31}^{(i)}}{\|\mathbf{Z}_1^{(i)}\|} & \frac{z_{32}^{(i)}}{\|\mathbf{Z}_2^{(i)}\|} & \frac{z_{33}^{(i)}}{\|\mathbf{Z}_3^{(i)}\|} \\ \frac{z_{41}^{(i)}}{\|\mathbf{Z}_1^{(i)}\|} & \frac{z_{42}^{(i)}}{\|\mathbf{Z}_2^{(i)}\|} & \frac{z_{43}^{(i)}}{\|\mathbf{Z}_3^{(i)}\|} \\ \frac{z_{51}^{(i)}}{\|\mathbf{Z}_1^{(i)}\|} & \frac{z_{52}^{(i)}}{\|\mathbf{Z}_2^{(i)}\|} & \frac{z_{53}^{(i)}}{\|\mathbf{Z}_3^{(i)}\|} \\ \frac{z_{61}^{(i)}}{\|\mathbf{Z}_1^{(i)}\|} & \frac{z_{62}^{(i)}}{\|\mathbf{Z}_2^{(i)}\|} & \frac{z_{63}^{(i)}}{\|\mathbf{Z}_3^{(i)}\|} \end{bmatrix}. \quad (C7)$$

Appendix D

Eq. (19) is equivalent to:

$$\mathbf{M}\mathbf{u} - \mathbf{C}^T \mathbf{h}_0^n + \mathbf{D}^T \mathbf{h}_f^n = \rho_r \mathbf{z} + \mathbf{g}^D, \quad (D1a)$$

$$\mathbf{C}\mathbf{u} + \mathbf{J}\mathbf{h}_0^n = \mathbf{Q} + \mathbf{S}_s \frac{\mathbf{h}_0^{n-1}}{\Delta t}, \quad (D1b)$$

$$\mathbf{D}\mathbf{u} = \mathbf{g}^N. \quad (D1c)$$

Using successive Schur-complement reduction (Maryška et al., 2000), first we left-multiply (D1a) by \mathbf{M}^{-1} yields:

$$\mathbf{u} = \mathbf{M}^{-1} \mathbf{C}^T \mathbf{h}_0^n - \mathbf{M}^{-1} \mathbf{D}^T \mathbf{h}_f^n + \mathbf{M}^{-1} (\rho_r \mathbf{z} + \mathbf{g}^D). \quad (D2)$$

Inserting (D2) into (D1b) and (D1c), \mathbf{u} can be eliminated:

$$(\mathbf{C}\mathbf{M}^{-1} \mathbf{C}^T + \mathbf{J}) \mathbf{h}_0^n - \mathbf{C}\mathbf{M}^{-1} \mathbf{D}^T \mathbf{h}_f^n = \mathbf{Q} + \mathbf{S}_s \frac{\mathbf{h}_0^{n-1}}{\Delta t} - \mathbf{C}\mathbf{M}^{-1} (\rho_r \mathbf{z} + \mathbf{g}^D), \quad (D3a)$$

$$\mathbf{D}\mathbf{M}^{-1} \mathbf{C}^T \mathbf{h}_0^n - \mathbf{D}\mathbf{M}^{-1} \mathbf{D}^T \mathbf{h}_f^n = -\mathbf{D}\mathbf{M}^{-1} (\rho_r \mathbf{z} + \mathbf{g}^D) + \mathbf{g}^N. \quad (D3b)$$

Similarly, since \mathbf{C} is block diagonal, $\mathbf{C}\mathbf{M}^{-1} \mathbf{C}^T + \mathbf{J}$ is block diagonal and invertible. We left-multiply (D3a) by $(\mathbf{C}\mathbf{M}^{-1} \mathbf{C}^T + \mathbf{J})^{-1}$:

$$\mathbf{h}_0^n = (\mathbf{C}\mathbf{M}^{-1} \mathbf{C}^T + \mathbf{J})^{-1} \mathbf{C}\mathbf{M}^{-1} \mathbf{D}^T \mathbf{h}_f^n + (\mathbf{C}\mathbf{M}^{-1} \mathbf{C}^T + \mathbf{J})^{-1} \times \left(\mathbf{Q} + \mathbf{S}_s \frac{\mathbf{h}_0^{n-1}}{\Delta t} - \mathbf{C}\mathbf{M}^{-1} (\rho_r \mathbf{z} + \mathbf{g}^D) \right). \quad (D4)$$

we denote:

$$\mathbf{H} = (\mathbf{C}\mathbf{M}^{-1} \mathbf{C}^T + \mathbf{J})^{-1} \mathbf{C}\mathbf{M}^{-1} \mathbf{D}^T, \quad (D5a)$$

$$\mathbf{G} = (\mathbf{C}\mathbf{M}^{-1} \mathbf{C}^T + \mathbf{J})^{-1} \left(\mathbf{Q} + \mathbf{S}_s \frac{\mathbf{h}_0^{n-1}}{\Delta t} - \mathbf{C}\mathbf{M}^{-1} (\rho_r \mathbf{z} + \mathbf{g}^D) \right), \quad (D5b)$$

(D4) can be rewritten as:

$$\mathbf{h}_0^n = \mathbf{H}\mathbf{h}_f^n + \mathbf{G}, \quad (D6)$$

Inserting (D6) into (D3b) gives:

$$(\mathbf{D}\mathbf{M}^{-1} \mathbf{C}^T \mathbf{H} - \mathbf{D}\mathbf{M}^{-1} \mathbf{D}^T) \mathbf{h}_f^n = -\mathbf{D}\mathbf{M}^{-1} \mathbf{C}^T \mathbf{G} - \mathbf{D}\mathbf{M}^{-1} (\rho_r \mathbf{z} + \mathbf{g}^D) + \mathbf{g}^N. \quad (D7)$$

Rather than solving Eq. (19) directly, we can now first solve (D7), insert the solution \mathbf{h}_f^n into (D6) to obtain \mathbf{h}_0^n , and finally use \mathbf{h}_f^n and \mathbf{h}_0^n in (D2) to obtain the total discharge \mathbf{u} .

References

- Aarnes, J.E., Krogstad, S., Lie, K.A., 2008. Multiscale mixed/mimetic methods on corner-point grids. *Comput. Geosci.* 12 (3), 297–315.
- Avavatsmark, I., Barkve, T., Bøe, Ø., Mannseth, T., 1996. Discretization on non-orthogonal, quadrilateral grids for inhomogeneous, anisotropic media. *J. comput. phys.* 127 (1), 2–14.
- Avavatsmark, I., Eigestad, G.T., Mallison, B.T., Nordbotten, J.M., 2008. A compact multipoint flux approximation method with improved robustness. *Numerical Methods Partial Differential Equations* 24 (5), 1329–1360.
- Agélas, L., Di Pietro, D.A., Droniou, J., 2010. The G method for heterogeneous anisotropic diffusion on general meshes. *ESAIM: Math. Model. Numerical Anal.* 44 (04), 597–625.
- Aghighi, M.A., Rahman, S.S., 2010. Horizontal permeability anisotropy: Effect upon the evaluation and design of primary and secondary hydraulic fracture treatments in tight gas reservoirs. *J. Petroleum Sci. Eng.* 74 (1), 4–13.
- Alpak, F.O., 2010. A mimetic finite volume discretization method for reservoir simulation. *SPE Journal* 15 (2), 436–453.
- Anderson, E., Bai, Z., Bischof, C., Blackford, S., Demmel, J., Dongarra, J., Du Croz, J., Greenbaum, A., Hammerling, S., McKenney, A., Sorensen, D., 1999. LAPACK Users' guide, Vol. 9. SIAM.
- Arbogast, T., Dawson, C.N., Keenan, P.T., 1995. Technical report CRPC-TR94392. RICE UNIVERSITY.
- Arbogast, T., Wheeler, M.F., Yotov, I., 1997. Mixed finite elements for elliptic problems with tensor coefficients as cell-centered finite differences. *SIAM J. Numerical Anal.* 34 (2), 828–852.
- Arnaldsson, A., Berhet, J.C., Kjaran, S., Sigurðsson, S.P., 2014. Numerical scheme to simulate flow through anisotropic rocks in TOUGH2. *Comput. Geosci.* 65, 37–45.
- Aziz, K., Settari, A., 1979. *Petroleum Reservoir Simulation*. Chapman & Hall.
- Bear, J., 1972. *Dynamics of Fluids in Porous Media*. Dover, New York.
- Bolton, A.J., Maltman, A.J., Fisher, Q., 2000. Anisotropic permeability and bimodal pore-size distributions of fine-grained marine sediments. *Mar. Petroleum Geology* 17 (6), 657–672.
- Brezzi, F., Fortin, M., 1991. *Mixed and Hybrid Finite Element Methods*. Springer-Verlag, New York.
- Brezzi, F., Douglas Jr., J., Marini, L.D., 1985. Two families of mixed finite elements for second order elliptic problems. *Numerische Math.* 47 (2), 217–235.
- Brezzi, F., Douglas Jr., J., Durán, R., Fortin, M., 1987a. Mixed finite elements for second order elliptic problems in three variables. *Numerische Math.* 51 (2), 237–250.
- Brezzi, F., Douglas Jr., J., Fortin, M., Marini, L.D., 1987b. Efficient rectangular mixed finite elements in two and three space variables. *RAIRO-Modélisation math. anal. numérique* 21 (4), 581–604.
- Brezzi, F., Lipnikov, K., Simoncini, V., 2005. A family of mimetic finite difference methods on polygonal and polyhedral meshes. *Math. Models Methods Appl. Sci.* 15 (10), 1533–1551.
- Chen, T., Clauser, C., Marquart, G., Willbrand, K., Mottaghy, D., 2015. A new upscaling method for fractured porous media. *Adv. Water Resources* 80, 60–68.
- Chen, Q.Y., Wan, J., Yang, Y., Mifflin, R.T., 2008a. Enriched multi-point flux approximation for general grids. *J. Comput. Phys.* 227 (3), 1701–1721.
- Chen, Y., Mallison, B.T., Durlofsky, L.J., 2008b. Nonlinear two-point flux approximation for modeling full-tensor effects in subsurface flow simulations. *Comput. Geosci.* 12 (3), 317–335.
- Chen, Z., Douglas Jr., J., 1989. Prismatic mixed finite elements for second order elliptic problems. *Calcolo* 26 (2–4), 135–148.
- Clauser, C., 1992. Permeability of crystalline rocks. *Eos, Trans. Am. Geophysical Union* 73 (21), 233–238.
- Clauser, C. (Ed.), 2003. *Numerical Simulation of Reactive Flow in Hot Aquifers: SHEMAT and Processing SHEMAT*. Springer, Heidelberg-Berlin.
- Cockburn, B., Gopalakrishnan, J., Lazarov, R., 2009. Unified hybridization of discontinuous Galerkin, mixed, and continuous Galerkin methods for second order elliptic problems. *SIAM J. Numerical Anal.* 47 (2), 1319–1365.
- Dickson, N.E.M., Comte, J.C., McKinley, J., Ofterdinger, U., 2014. Coupling ground and airborne geophysical data with upscaling techniques for regional groundwater modeling of heterogeneous aquifers: Case study of a sedimentary aquifer intruded by volcanic dykes in Northern Ireland. *Water Resources Res.* 50 (10), 7984–8001.
- Domenico, P.A., Schwartz, F.W., 1998. *Physical and Chemical Hydrogeology*, Vol. 44. Wiley, New York.
- Droniou, J., 2014. Finite volume schemes for diffusion equations: Introduction to and review of modern methods. *Math. Models Methods Appl. Sci.* 24 (08), 1575–1619.
- Durlofsky, L.J., 2005. Upscaling and gridding of fine scale geological models for flow simulation. 8th International Forum on Reservoir Simulation, Iles Borromées.
- Edwards, M.G., Rogers, C.F., 1998. Finite volume discretization with imposed flux continuity for the general tensor pressure equation. *Comput. Geosci.* 2 (4), 259–290.
- Farrell, N.J.C., Healy, D., Taylor, C.W., 2014. Anisotropy of permeability in faulted porous sandstones. *J. Struct. Geology* 63, 50–67.
- Gessner, K., Kühn, M., Rath, V., Kosack, C., Blumenthal, M., Clauser, C., 2009. Coupled process models as a tool for analysing hydrothermal systems. *Surveys geophysics* 30 (3), 133–162.
- Koudina, N., Garcia, R.G., Thovert, J.F., Adler, P.M., 1998. Permeability of three-dimensional fracture networks. *Phys. Rev. E* 57 (4), 4466.
- Hsieh, P.A., Neuman, S.P., 1985. Field determination of the three-dimensional hydraulic conductivity tensor of anisotropic media: 1. theory. *Water Resources Res.* 21 (11), 1655–1665.
- Hu, B.X., Meerschaert, M.M., Barrash, W., Hyndman, D.W., He, C., Li, X., Guo, L., 2009. Examining the influence of heterogeneous porosity fields on conservative solute transport. *J. Contam. Hydrol.* 108 (3), 77–88.
- Kumar, A., Noh, M.H., Ozah, R.C., Pope, G.A., Bryant, S.L., Sepehrnoori, K., Lake, L.W., 2005. Reservoir simulation of CO₂ storage in aquifers. *SPE Journal* 10 (03), 336–348.
- Lee, S.H., Lough, M.F., Jensen, C.L., 2001. Hierarchical modeling of flow in naturally fractured formations with multiple length scales. *Water Resources Res.* 37 (3), 443–455.
- Lewis, J.J.M., 1988. Outcrop-derived quantitative models of permeability heterogeneity for genetically different sand bodies. SPE Annual Technical Conference and Exhibition. Society of Petroleum Engineers.
- Li, L., Zhou, H., Jaime Gómez-Hernández, J., 2010. Steady-state saturated groundwater flow modeling with full tensor conductivities using finite differences. *Comput. Geosciences* 36 (10), 1211–1223.
- Lie, K.A., Krogstad, S., Ligaarden, I.S., Natvig, J.R., Nilsen, H.M., Skaflestad, B., 2012. Open-source MATLAB implementation of consistent discretisations on complex grids. *Comput. Geosciences* 16 (2), 297–322.
- Lipnikov, K., Manzini, G., Shashkov, M., 2014. Mimetic finite difference method. *J. Comput. Phys.* 257, 1163–1227.
- Lipnikov, K., Moulton, J.D., Svyatskiy, D., 2011. Adaptive strategies in the multilevel multiscale mimetic (M³) method for two-phase flows in porous media. *Multiscale Model. Simulation* 9 (3), 991–1016.
- Llanos, E.M., Zarrouk, S.J., Hogarth, R.A., 2015. Numerical model of the Habanero geothermal reservoir, Australia. *Geothermics* 53, 308–319.
- Lunde, T., 2007. Comparison Between Mimetic and Two-Point Flux-Approximation Schemes on PEBI-Grids Master thesis. University of Oslo.
- Makse, H.A., Havlin, S., Ivanov, P.C., King, P.R., Prakash, S., Stanley, H.E., 1996. Pattern formation in sedimentary rocks: connectivity, permeability, and spatial correlations. *Phys. A: Stat. Mech. Appl.* 233 (3), 587–605.
- Manga, M., Beresnev, I., Brodsky, E.E., Elkhouri, J.E., Elsworth, D., Ingebretsen, S.E., Mays, D.C., Wang, C.Y., 2012. Changes in permeability caused by transient stresses: field observations, experiments, and mechanisms. *Rev. Geophys.* 50 (2), RG2004.
- Maryška, J., Rozložník, M., Tůma, M., 2000. Schur complement systems in the mixed-hybrid finite element approximation of the potential fluid flow problem. *SIAM Journal on Scientific Computing* 22 (2), 704–723.
- McKenna, S.A., Walker, D.D., Arnold, B., 2003. Modeling dispersion in three-dimensional heterogeneous fractured media at Yucca Mountain. *J. contam. hydrol.* 62, 577–594.
- Meyer, R., Krause, F.F., 2006. Permeability anisotropy and heterogeneity of a sandstone reservoir analogue: An estuarine to shoreface depositional system in the Virgelle Member, Milk River Formation, Writing-on-Stone Provincial Park, southern Alberta. *Bulletin Can. petroleum geology* 54 (4), 301–318.
- Miller, C.T., Dawson, C.N., Farthing, M.W., Hou, T.Y., Huang, J., Kees, C.E., Kelley, C.T., Langtangen, H.P., 2013. Numerical simulation of water resources problems: models, methods, and trends. *Adv. Water Resources* 51, 405–437.
- Min, K.B., Rutqvist, J., Tsang, C.F., Jing, L., 2004. Stress-dependent permeability of fractured rock masses: a numerical study. *Int. J. Rock Mech. Mining Sci.* 41 (7), 1191–1210.
- Nédélec, J.C., 1980. Mixed finite elements in \mathbb{R}^3 . *Numerische Math.* 35 (3), 315–341.
- Neupauer, R.M., Powell, K.L., Qi, X., Lee, D.H., Villhauer, D.A., 2006. Characterization of permeability anisotropy using wavelet analysis. *Water Resources Res.* 42 (7), W07419.
- Nikitin, K., Terekhov, K., Vassilevski, Y., 2014. A monotone nonlinear finite volume method for diffusion equations and multiphase flows. *Comput. Geosci.* 18 (3–4), 311–324.
- Nilsen, H.M., Lie, K.-A., Natvig, J.R., 2012. Accurate modelling of faults by multipoint, mimetic, and mixed methods. *SPE Journal* 17 (2), 568–579.
- Nordbotten, J.M., Eigestad, G.T., 2005. Discretization on quadrilateral grids with improved monotonicity properties. *J. comput. phys.* 203 (2), 744–760.
- Papadopoulos, I.S., 1965, September. Nonsteady flow to a well in an infinite anisotropic aquifer. In: Proceedings of the Dubrovnik Symposium on the Hydrology of Fractured Rocks. International Association of Scientific Hydrology, pp. 21–31.
- Renard, P., Genty, A., Stauffer, F., 2001. Laboratory determination of the full permeability tensor. *J. Geophys. Res.* 106 (811), 26443–26452.
- Rath, V., Wolf, A., Bücker, H.M., 2006. Joint three-dimensional inversion of coupled groundwater flow and heat transfer based on automatic differentiation: sensitivity calculation, verification, and synthetic examples. *Geophys. J. Int.* 167 (1), 453–466.
- Raviart, P.A., Thomas, J.M., 1977. A mixed finite element method for 2-nd order elliptic problems. In: *Mathematical Aspects of Finite Element Methods*. Springer, Berlin Heidelberg, pp. 292–315.
- Sandve, T.H., Berre, I., Nordbotten, J.M., 2012. An efficient multi-point flux approximation method for discrete fracture–matrix simulations. *J. Comput. Phys.* 231 (9), 3784–3800.
- Shashkov, M., Steinberg, S., 1996. Solving diffusion equations with rough coefficients in rough grids. *J. Comput. Phys.* 129 (2), 383–405.
- Snow, D.T., 1969. Anisotropic permeability of fractured media. *Water Resources Res.* 5 (6), 1273–1289.
- Srinivasan, S., Azom, P.N., 2013. Modeling the effect of permeability anisotropy on the steam-assisted gravity drainage (SAGD) process in multi-layered reservoirs. SPE Heavy Oil Conference-Canada. Society of Petroleum Engineers.
- Verma, S., Aziz, K., 1997. A control volume scheme for flexible grids in reservoir simulation. SPE Reservoir Simulation Symposium. Society of Petroleum Engineers.

- Wright, H.M., Cashman, K.V., Gottesfeld, E.H., Roberts, J.J., 2009. Pore structure of volcanic clasts: measurements of permeability and electrical conductivity. *Earth Planetary Sci. Lett.* 280 (1), 93–104.
- Zhang, D., Zhang, R., Chen, S., Soll, W.E., 2000. Pore scale study of flow in porous media: Scale dependency, REV, and statistical REV. *Geophys. Res. Lett.* 27 (8), 1195–1198.
- Zhang, F. (Ed.), 2006. The Schur Complement and its Applications. Springer, New York.
- Zhang, S., Tullis, T.E., 1998. The effect of fault slip on permeability and permeability anisotropy in quartz gouge. *Tectonophysics* 295 (1), 41–52.
- Zijl, W., 1996. The symmetry approximation for nonsymmetric permeability tensors and its consequences for mass transport. *Transport porous media* 22 (2), 121–136.
- Zijl, W., 1999. Scale aspects of groundwater flow and transport systems. *Hydrogeol. J.* 7 (1), 139–150.